Gemeda *et al.*
Journal of Engineering and Applied Science (2024) 71:116
https://doi.org/10.1186/s44147-024-00436-4

Journal of Engineering and Applied Science

RESEARCH Open Access

Optimization of porosity behavior of hybrid reinforced titanium metal matrix composite through RSM, ANN, and GA for multi-objective parameters

Birhane Assefa Gemeda[1], Devendra Kumar Sinha[1*], Getinet Asrat Mengesha[2] and Satyam Shivam Gautam[3]

*Correspondence:
devendrasinhame@astu.edu.et

[1] Mechanical Engineering Department, School of Mechanical, Chemical and Materials Engineering, Center of Excellence Advanced Manufcaturing Engineering,, Adama Science &Technology University, Adama, Ethiopia
[2] Department of Materials Science and Engineering, Adama Science & Technology University, Adama, Ethiopia
[3] Mechanical Engineering Department, North Eastern Regional Institute of Science and Technology, Itanagar, Arunachal Pradesh 791109, India

Abstract

Titanium matrix composites (TMCs) have high specific strength and stiffness, and high-temperature TMCs can reduce weight by up to 50% when compared with monolithic super alloys while preserving equal stiffness and strength in jet engine systems for propulsion. The purpose of this work examines the use of mathematical models and learning approaches to optimize response such as porosity and control variables in synthesized hybrid titanium metal matrix composites (HTMMCs) reinforced by B_4C-SiC-MoS_2-ZrO_2. To further understand the impacts of process factors on porosity reduction, the study employs methodologies such as the response surface methodology (RSM), integrated artificial neural networks (ANN), and genetic algorithm (GA). The findings indicate that these strategies have the potential to contribute to the industry. The optimal combination of 7.5wt.% SiC, 7.5wt.% B_4C, 7.5wt.% ZrO_2, 4wt.% MoS_2, and 73.5wt.% Ti compositions was determined utilizing process factors such as milling period (6h), compaction pressure (50MPa), compact duration (50min), sintering temperature (1200°C), and sintering time (2h) as compared to pure Ti grade 5. The mechanical properties of the optimum combination of reinforcement weight percentage and process parameters resulted in a minimum porosity of 0.118%, density of 4.36gcm^3, and micro-hardness of 63.4HRC boosted by 1.76%, and compressive strength of 2500MPa increased by 2.6%. In addition, these HTMMCs had a minimal wear rate of 0.176mm^3/Nm and a corrosion resistance rate of 2.15×10-4mmpy. The investigation result analysis discovered that the RSM and combined ANN-GA models considerably enhanced the forecasting of multidimensional interaction difficulties in composite material production that were highly statistically connected, with R^2 values of 0.9552 and 0.97984. The ANN-GA model provided a 95% confidence range for porosity predictions, which increased the production use of titanium-based particle composites. Furthermore, HMMCs can be utilized in the automotive and aviation industries with enhanced corrosion and wear resistance.

Keywords: Hybrid titanium metal matrix composite, Porosity, Response surface methodology, Artificial neural networks, Genetic algorithm

Introduction

The aerospace and automotive industries are currently experiencing a massive increase in demand for novel technological materials, particularly metal matrix composites (MMCs). Titanium, a lightweight metal, is inappropriate owing to its low strength, wear resistance, and hardness. Efforts in research and development attempt for the enhancement of mechanical, physical, and other the characteristics of composite for engineering materials [1].

Titanium and its alloys were formidable to produce because of their brittle nature, lower resistance wear, and high manufacturing costs. The researchers want to make titanium and its alloys more affordable and in great demand for the transportation, automotive, and aviation industries. They are looking for ways to lower production costs while improving performance through the use of low-cost and harder ceramic reinforcements. They are improving mechanical properties and lowering production costs by combining nanoparticles and conventional composites. This one-of-a-kind technology seeks to enhancement of durability and performance within titanium metal and alloys [2–4].

Manufacturing improvements in technology, material characterization, and the morphology govern are critical for enhancing mechanical and thermal characteristics. Ti6Al4V, a prominent titanium matrix material, is limited in its applicability because of its poor wear resistance and surface hardness. Nonetheless, titanium alloys have poor tribological performance, with characteristics like an elevated and inconsistent coefficient of friction, excessive wear adhesive, and susceptibility to concerned wear rate that is viewed to be a serious drawback that limits their applicability [5].

MMCs have attracted the focus and consideration of researchers during the last 40 years owing to their application and versatile properties like outstanding resistance to abrasion, specific strength, and thermal endurance, attracting a several scientists to be created and prepared to satisfy the industry's demands regarding engineering material requirements. According to research, lowering the size of the reinforcement particles, notably from micrometers to nanometers, can greatly improve the mechanical characteristics of MMCs, particularly in nanocomposites [6].

Hybrid titanium metal matrix composites (HTMMCs) are prominent because of their superior mechanical and physical qualities, which include increased strength, lightweight, high stiffness, superior wear resistance, extremely greater strength-to-weight ratio, and an excellent elastic modulus. These composites are made by combining different materials to improve various qualities such as enhanced structural and mechanical characteristics, tribological properties, chemical, thermal, wear, and corrosion resistance behavior [7].

Many whiskers, particulates, and fiber materials such as ceramics have been proposed for optimizing the properties of HTMMCs, incorporating SiC, rare earth oxides, B_4C, Ti_5Si_3, TiO_2, TiC, Y_2O_3, nanodiamonds, TiB, graphene nanoplatelets, MoS_2, WC, and ZrO_2. The type of reinforcement is decided according to the materials' designed performance purpose along with industrial requirements [8]. Because of their favorable integration with matrix alloys, B_4C, SiC, MoS_2, and ZrO_2 are appropriate reinforcements for titanium base metal, improving friction, corrosion and wear resistance, hardness, and durability.

Preparing uniformly distributed nanoparticles remains difficult due to the enormous van der Waals adhesive force, which causes spontaneous agglomeration and inconsistent microstructure. Traditional materials fabrication methods, consisting of as casting and high-pressure sintering, mimic this dispersion or spatial arrangement, maintaining nanoscale grains after the procedure [6, 9].

Powder metallurgy (PM) is a low-cost, high-precision, near-net form manufacturing technique for making high-performance, complex-shaped components. Because of its homogeneity and minimal pores, it is a highly efficient approach of providing in situ material manufacture. PM uses milling, compaction, and sintering to generate, consolidate, and amalgamate engineered material components [10].

Multi-objective optimization is the systematic and simultaneous optimization multiple objective functions, with an emphasis on engineering applications. The fundamental purpose is to represent decision-makers' preferences, and approaches are classified according to how they communicate these preferences. Multi-objective optimization issues are converted into single-objective optimization using a variety of optimization analysis approaches. This comprehensive overview examines approaches and their amendments [11–13]. Moreover, RSM optimizes the objective function and may mislead the results by yielding the local optimum value of the response variable whereas GA always yields the global optimum value of the response variable.

The numerous optimization strategies are employed to enhance and optimize efficiency and effectiveness though various methods, such as Taguchi, GA, RSM, Grey Taguchi, and ANN [1].

Process factor optimization is critical for conserving resources, materials, and money in experimental activity. Advanced statistical methods, like the RSM, were required to analyze complicated processes with various input variables [14]. Minimal experiments can be used to develop map domains adopting RSM. Despite extensive optimization for robust processes, BOX BEHNKEN provides greater insight and necessitates a lesser amount runs of experiments [15].

ANN is computer programs that simulate nerve cell connections across the nervous system on a neuron-by-neuron and element-by-element basis. Researchers are using ANN to predict response behaviors in newly manufactured composites, which represent a significant boost in the usage of artificial intelligence within application of engineering. In modeling and addressing linear and nonlinear engineering issues, ANN can give complicated interactions between variables that are input and output, potentially substituting polynomial regression [16, 17].

For multi-objective optimizations, the GA was utilized, with non-linear regression and Buckingham's pi theorem models demonstrating strong modeling abilities over the parameters of the process [18]. To improve the mechanical characteristics and responses of hybrid composite structures, a multi-objective GA and a resilient design technique were used [19].

Researchers can optimize control variables and response porosity in hybrid nanoparticles reinforced by B_4C-SiC-MoS_2-ZrO_2/Ti composites using mathematical models and learning approaches. To forecast control variables and response porosity, this study employs RSM and integrated ANN-GA. The study focuses on the interaction

Table 1 Ti grade 5 chemical constituent/composition

Element	Al	V	O	N	H	Zr	Fe	Ti
Wt. %	6.2	4.35	0.55	0.5	0.3	0.03	0.02	Balance

Table 2 Physical and mechanical attributes of titanium grade five

S. No.	Properties	Measured value/amount	S. No.	Properties	Measured value/amount
1	Density	4.43 g/cm^3	11	Reduction of area	36%
2	Hardness, Rockwell C	36	12	Elongation at break	14%
3	Hardness, Brinell	334	13	Modulus of elasticity	113.8 GPa
4	Hardness, Vickers	349	14	Notched tensile strength	1450 MPa
5	Hardness, Knoop	363	15	Bearing yield strength	1480 MPa
6	Tensile strength, ultimate	950 MPa	16	Ultimate bearing strength	1860 MPa
7	Compressive yield strength	970 Mpa	17	Fatigue strength	510 MPa
8	Tensile strength, yield	880 MPa	18	Poisson's ratio	0.342
9	Charpy impact	17 J	19	Fracture toughness	75 MPa-m½
10	Shear modulus	44 GPa	20	Shear strength	550 MPa

impacts of process factors on porosity minimization, which is a rare comparison of various strategies.

The research investigation focuses to determine how reinforcing content and process factors affect Ti-SiC-B_4C-ZrO_2-MoS_2 composite porosity. Empirical models include RSM and integrated ANN-GA predictive models, with ANN used to predict response. RSM examines dependability in complicated engineering, whereas GA optimizes using natural selection and genetics.

Methods

Raw material

Grade 5 titanium 80μm, B_4C 53nm, SiC 37 nm, MoS_2 97nm, and ZrO_2 85nm nanoparticles with sizes and all composition purity >99% were obtained from SAVEER MATRIX NANO PVT. LTD, Uttar Pradesh, India. PM was used to make nanocomposites of Ti-B_4C, SiC, MoS_2, and ZrO_2. Mechanical parameters of optimum specimen such as densification, porosity, the influence of sintered temperature, hardness, and reinforcing dimensions dependency and dispersion were examined. The reinforcement (2.5, 5, 7.5%) Wt.% of B_4C, SiC, and ZrO_2 developed experiment combination, 4% MoS_2, and titanium as balance. A homogenous blend of matrix and reinforcements in three-level combinations was developed for investigational purposes. PM was utilized to generate nanocomposites such as Ti-B_4C, SiC, MoS_2, and ZrO_2, and mechanical features such as densification, microstructure, and reinforcement size dependence were investigated. Powder mixing, cold compression, and sintering are examples of traditional PM processes. Tables 1 and 2 clearly show the composition of chemicals as well as the physical and mechanical properties of Ti grade 5, providing comparison of the current investigation's results.

Powder metallurgy method

A FRITSCH high ball mill from Germany was used to produce the distinct Wt.% (7.5, 5, 2.5%) Wt.% of B_4C, SiC, and ZrO_2, as well as an additional 4% MoS_2-reinforced Ti composite powder. The rotating speed was 250rpm and the powder to ball ratio (PBR) was 1:10.

The combined particles were squeezed into 10 mm diameter and 12 mm length cylinder-shaped pellets within a hydraulic pallet pressing under a compression pressure of 40, 45, and 50MPa using unidirectional, compression dies. The green body was sintered within an appropriately controlled environment using an electric furnace containing a flow regulator at temperatures of (800, 1000, and 1200°C) for (1, 1.5, and 2 h), respectively. Sintering was carried out using a constant circulation of argon gas with an intake rate equal to 0.5 L/min to prevent manufactured composites specimen from oxidizing. Throughout the furnace, the sintered pellets underwent cooling to room temperature. As seen in Fig. 1, the method of fabricating HTMMCs consists of (a) powdered raw material particles and (b) sintered samples obtained through the powder metallurgy process.

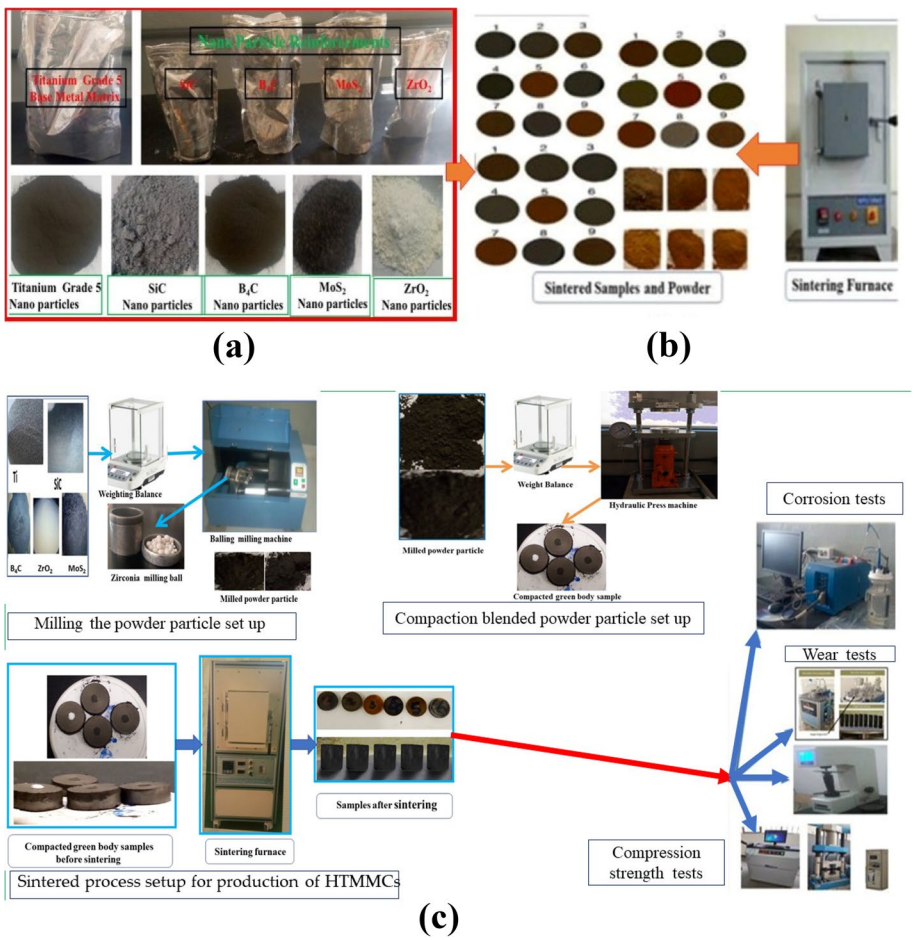

Fig. 1 The process of fabricating HTMCs. **a** Powder raw material particles; **b** sintering samples; **c** experimental setup for the synthesis using powder metallurgy process and testing

Testing and characterization

To explore the morphology of a material, the Jeol Japan SEM, Model JCM/6000PLUS BENCH TOP SEM, Musashino, Akishima, Tokyo 196-8558, Japan, was employed. For the purpose of determining the presence of reinforcing particles, X-ray diffractometer (XRD) was performed on fabricated synthesized composites using an XRD-7000 maxima (Shimadzu Corporation, Japan, Tokyo). CuKa radiation ($k = 1.5406$ A)^0 combined 40kV working voltages and 40 mA current was used for maintaining a diffractometer. Regarding thorough assessment of all existing phases, data from XRD was collected at a slow scanning rate of 0.02 steps/s. The scanning capability and frequencies were 10^0 to 85^0 in 0.02^0 step increments. Fourier transform infrared (FTIR) was obtained using the Bruker-alpha-FTIR spectrometer (Bruker Corporation, Billerica, MA, USA) in attenuation full reflection mode. A digital Rockwell micro-hardness type HRS-150, Beijing United Tester Co., LTD of Beijing, China, was also used for micro-hardness measuring device testing, with a weight of 150kgf and a holding time of 15 s. During the hardness test, the probable error due to experimentation was less than 5%. The test was performed at ambient temperature, the measurements of hardness were obtained four times per every specimen tested at various sites, and the average results were used to calculate micro-hardness. The sintered porosity of all manufactured composite samples was measured experimentally using the Archimedes' principle and a standard test protocol (ASTM-B0311-93R02E01). An analytical balance was used to determine the sintered porosity of composites using Archimedes' technique to test specimens to approximate their porosity. The sintered weight occurring into specimens were initially assessed with the support and aid of a precise digital weighing balance (HR-250AZ, A&D Company Limited, Korea) with a 0.0001gm accuracy.

Experimental design

For the model formation within RSM, the BOX BEHNKEN techniques were adopted to investigate the independent and the effects interaction within multivariable on the porosity of composite produced samples (B_4C, SiC, MoS_2, and ZrO_2) Wt.% concentrations and process parameter (sintering temperatures and time, compaction pressure and time, milling time) circumstances. The goal of using BOX BEHNKEN to the parameters utilized throughout this study is to create the 2nd-order model effectively; BOX BEHNKEN designs are enhanced with additional center and axial locations to allow estimation of the governing factors of a second-order model. The provided input characteristics/factors were multifactorial (Wt.% of concentrations of B_4C, SiC, MoS_2, and ZrO_2) and process variable (sintering temperatures and time, compaction pressure and time, milling time) circumstances; the process variables comprising lower and higher values have been indicated within Table 3. As presented through Table 4, the outcome factor/response variables were porosity. The explanations concerning the matrices of arrangement of the elements in the various units employed in the RSM, as well as the porosity responses, have been reported within Table 4.

Table 3 Variables of input and DOE levels prescribed specifications

No.	HTMMC optimization process parameters	Unit	Parameters designation	Type	Minimum	Maximum
1	Milling duration	Hrs.	MD	Numeric	4	6
2	Compaction pressure	MPa	CP	Numeric	40	50
3	Compaction duration	Minute	CD	Numeric	30	50
4	Sintering temperature	0C	ST	Numeric	800	1200
5	MoS_2 Wt.%	Wt.%	MoS_2	Numeric	4	4
6	SiC Wt.%	Wt.%	SiC	Numeric	2.5	7.5
7	B_4C Wt.%	Wt.%	B_4C	Numeric	2.5	7.5
8	ZrO_2 Wt.%	Wt.%	ZrO_2	Numeric	2.5	7.5

Table 4 Design matrix within runs of experimentation

Std	Run	Factor				Response
		Milling time (hrs.)	Compaction pressure (MPa)	Compaction time (Min.)	Sintering temperature (0C)	Porosity (%)
6	1	5	45	50	800	0.411
24	2	5	50	40	1200	0.531
5	3	5	45	30	800	0.432
16	4	5	50	50	1000	0.431
11	5	4	45	40	1200	0.265
7	6	5	45	30	1200	0.342
18	7	6	45	30	1000	0.341
25	8	5	45	40	1000	0.395
20	9	6	45	50	1000	0.384
13	10	5	40	30	1000	0.287
4	11	6	50	40	1000	0.139
2	12	6	40	40	1000	0.168
19	13	4	45	50	1000	0.391
23	14	5	40	40	1200	0.512
21	15	5	40	40	800	0.453
17	16	4	45	30	1000	0.167
10	17	6	45	40	800	0.357
27	18	5	45	40	1000	0.445
3	19	4	50	40	1000	0.374
8	20	5	45	50	1200	0.356
26	21	5	45	40	1000	0.444
14	22	5	50	30	1000	0.179
1	23	4	40	40	1000	0.323
22	24	5	50	40	800	0.267
15	25	5	40	50	1000	0.43
9	26	4	45	40	800	0.429
12	27	6	45	40	1200	0.471

Response surface methodology

The RSM was an effective method for analyzing robustness in complicated engineering with explicit boundary function states. Utilizing factorial techniques and ANOVA, it optimizes multifactorial parameter sets to reach desirable values. RSM

provides valuable data from small trials, which facilitates the analysis of principal outcomes and the effect they have on response. RSM, also known as response surface modeling, is a technique for optimizing responses when several quantitative elements are present [20].

Factorial research designs use three-level variables that are independent to demonstrate interaction between both independent and dependent variables. Homogeneously variation in choice parameters aids in understanding the impacts of variable levels on response, leading to optimum answers as shown in Fig. 2.

Integrated ANN-GA optimization technique

ANN has since been used in human cognition studies, with predictive models being critical for determining output. This research used MATLAB's ANN toolkit to develop neural network topologies, analyzing architecture, training technique, and activation function. Because of their ease of creation, efficiency, and simplicity, backpropagation neural networks are commonly used in applications involving engineering. Several models were created and evaluated to be capable of finding the major effective configuration design, training method, and activation operation functioning. An optimization algorithm, in general, is a form of intelligent approach used to discover the ideal casting conditions [21].

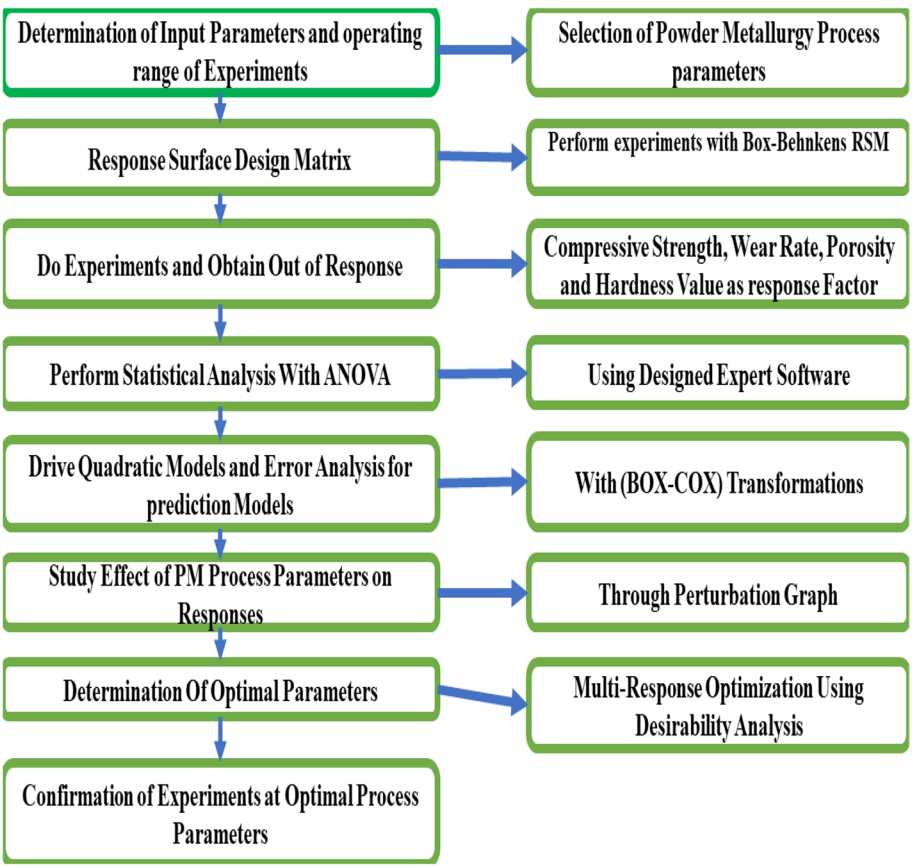

Fig. 2 A schematic representation of RSM approaches

Genetic algorithms (GAs) are search-based algorithms that use natural selection and genetics to solve optimization problems and alter solutions on a regular basis. They are iterative procedures that begin with a fixed-size population of candidate designs and progress through a fitness function for each member. GAs is noted for their clarity, refinement, efficacy, and independence from language. The function of fitness facilitates in selecting individuals from the general population, whereas crossover approaches specify the offspring produced [22]. The GAs is the most extensively used evolutionary optimization tool. Many researches [21, 23] use a combined method of ANN and GAs as evolutionary strategies to achieve multi-objective optimization. The integrated ANN-GA flow diagram in Fig. 3 clearly depicts the procedures and techniques employed throughout the present investigation to obtain the best engineering material and the most cost-effective HTMMs' developed samples.

Results and discussion

Porosity analysis

The optimum sample density of the produced composite material might vary depending upon the density associated with the reinforcement components, phase and dimension two-component combination, and production method and system. To approximate porosity, experimental density, and water absorption, Archimedes' method was applied to sintered samples. Reduced density is associated with fewer reinforcing particles and spaces. The Archimedes technique has been utilized to compute the weight of sintered, wet, and submerged material. As shown in Table 4, the design matrix is within the runs of experimentation and the porosity response of the outcome of the computed porosity of synthesized HTMMCS.

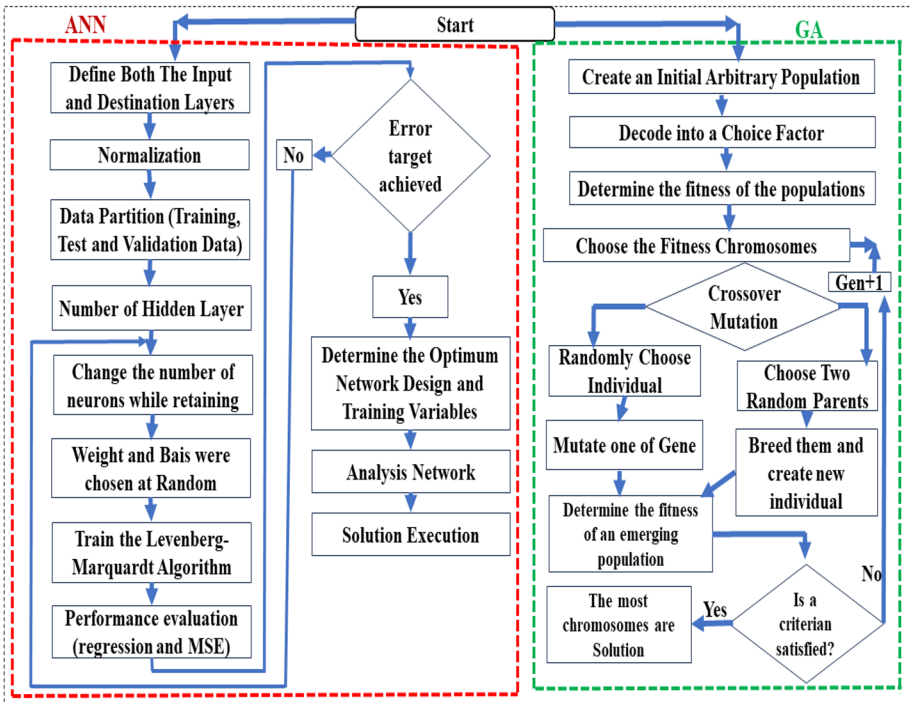

Fig. 3 Integrated ANN-GA flow diagram

Porosity rose in the composite fabrication as the mass fraction of SiC particles in the composition increased. The high relative density of sintered specimens (all optimum samples greater than 90% relative density) shows a strong/tough interface interacting between powder nanoparticles with little cavities/porosity. The void content of the synthesized HTMMCS was less than one in all samples, making this unique material appealing, and provides a broad spectrum of engineering requirements and purpose. This means that it was appropriate engineering materials for automotive and aeronautical applications. Furthermore, the produced specimen density was lower than the theoretical density observed due to the inclusion of low density reinforced hard ceramic particles such as SiC and B_4C. The lowest experimental density and porosity with the composition of 7.5% SiC, 7.5%B_4C, 4%MoS_2, 7.5%ZrO_2, and 73.5%Ti with the composition of fabricated sample are 11 of the result provided 4.259 g/cm^3 and 0.13%, respectively, as well as with 95.048% relative density.

RSM modeling

RSM models regarding porosity were developed combining experimental data and design experiments. A quadratic model including square, linear, and interaction terms for interaction was created using design expert software, and responses to input variables.

$$\mathrm{Y}(1) = 0.041\mathrm{X}_3 - 0.095{X^2}_1 - 0.06{X^2}_2 + 0.038{X^2}_4 \quad (1)$$

Table 5 shows the ANOVA table for porosity, from which Eq. (1) is derived. As shown, the F-values of the models all demonstrate that the proposed model is significant, with the exception of milling time, sintering temperature, and the interaction of "Milling

Table 5 ANOVA table for the porosity model

Source	DF	Seq SS	Adj SS	Adj MS	F	*P*
Regression	14	0.189332	0.189332	0.013524	18.29	0.000
Model	4	0.022883	0.022883	0.005721	7.74	0.003
Milling time	1	0.000008	0.000008	0.000008	0.01	0.917
Compaction pressure	1	0.001633	0.001633	0.001633	2.21	0.163
Compaction time	1	0.020833	0.020833	0.020833	28.17	0.000
Sintering temperature	1	0.000408	0.000408	0.000408	0.55	0.472
Square	4	0.090699	0.090699	0.022675	30.66	0.000
Milling time*milling time	1	0.045742	0.047712	0.047712	64.51	0.000
Compaction pressure*compaction pressure	1	0.0217	0.018148	0.018148	24.54	0.000
Compaction time*compaction time	1	0.015589	0.007837	0.007837	10.6	0.007
Sintering temperature*sintering temperature	1	0.007668	0.007668	0.007668	10.37	0.007
Interaction	6	0.07575	0.07575	0.012625	17.07	0.000
Milling time*compaction pressure	1	0.003025	0.003025	0.003025	4.09	0.066
Milling time*compaction time	1	0.0169	0.0169	0.0169	22.85	0.000
Milling time*sintering temperature	1	0.0289	0.0289	0.0289	39.08	0.000
Compaction pressure*compaction time	1	0.0049	0.0049	0.0049	6.63	0.024
Compaction pressure*sintering temperature	1	0.015625	0.015625	0.015625	21.13	0.001
Compaction time*sintering temperature	1	0.0064	0.0064	0.0064	8.65	0.012
Residual error	12	0.008875	0.008875	0.00074		
Lack-of-fit	10	0.008875	0.008875	0.000888	*	*
Pure error	2	0	0	0		
Total	26	0.198207				

Time*Compaction Pressure" at 95% assurance level of $P \leq 0.05$. The milling time, sintering temperature, and interaction of "Milling Time*Compaction Pressure" F-values of 0.917, 0.472, and 0.066, respectively, indicate that they are not significant. There is a 91.7%, 47.2%, and 6.6% possibility of milling duration, sintering temperature, and interaction of "Milling Time*Compaction Pressure" F-value; this big might occur owing to noise. These findings are consistent with earlier studies [24].

All among the four models listed in Table 6, the bold numbers reflect the most viable model indicated by the RSM tool, which is quadratic. The RSM was used for assessing and analyzing the results of the experiment collected from the BOX BEHNKEN, as indicated within Table 4. The current work's investigation was carried out using design expert software. Table 6 summarizes the porosity response model. Table 6 displays the adequacy metrics R^2, adjusted R^2, and anticipated R^2. All indications of sufficiency are in acceptable agreement and show a significant link. Because the difference is smaller than 0.1609, its predicted R^2 of 0.7421 correlates reasonable closely with the adjusted R^2 of 0.903. An analysis of variance result for the porosity model suggests that the primary influence of process variables (reinforcing particulate concentration and process parameter) as well as the interaction effect of the parameters are significant [24].

Implications of process parameter on porosity analysis

In recognition of conciseness, only the influence of process factors on porosity is discussed. Figures 4, 5, 6 and 7 depict the relationships between the porosity responsiveness and the variable in the method. Each figure within this research investigation extends and depicts the impact of process factors versus to another factor put and contributed the values at the central point. The response surface plot better illustrate each factor's capacity to influence porosity. According to Fig. 5 (a–c) (3D plot of response surface), the process variable (ranked as 1 compression pressure, 2 milling duration and 3 sintering temperature) has the greatest influence on the porosity of composites, subsequent reinforcement Wt.% concentration; this result coincided with result of previous investigation [25]. Furthermore, as shown in Fig. 7(a–c), increasing the value of each process variable (such as compression pressure and time, milling duration, sintering temperature, and time) significantly improves the porosity level score and is desired to keep at a minimum for quality and high-performance engineering material fabrication. The model reveals no sudden fluctuation in the continuous variance. The genuine information/data points throughout the graph are almost identical to the projected ones; the optimization demonstrates that the quadratic model was an effective approach model for determining the reaction rate of a factor an independent variable. Porosity reduces at 7.5%SiC, 7.5%B_4C, 4%MoS_2, 7.5%ZrO_2,

Table 6 Summarizes the response (porosity) model

Source	Std. Dev.	R^2	Adjusted R^2	Predicted R^2
Linear	2.27	0.3709	0.325	−0.4605
2FI	2.53	0.376	0.0547	−1.9243
Quadratic	**0.10558**	**0.9552**	**0.903**	**0.7421**
Cubic	1.51	0.8176	0.7022	0.7891

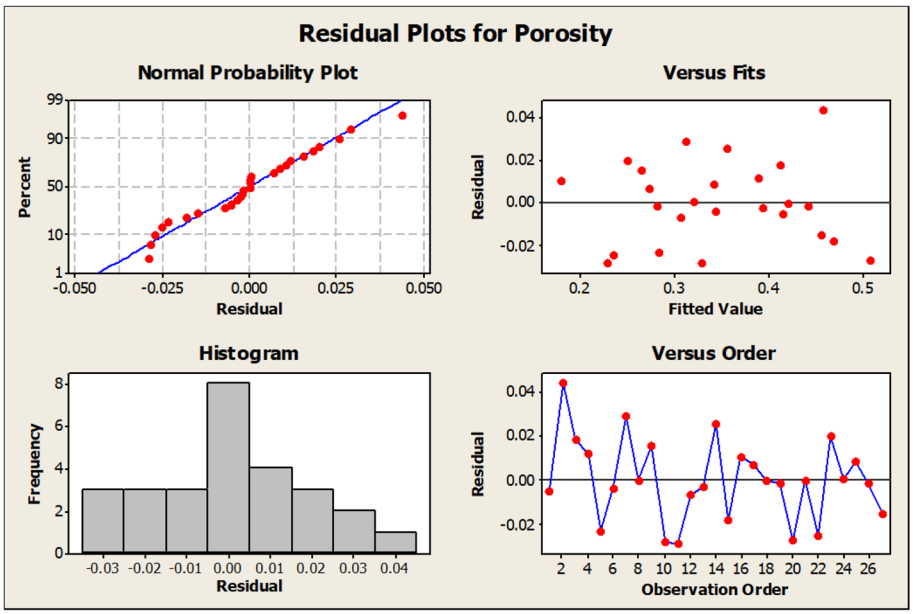

Fig. 4 Residual plots for porosity analysis

and 73.5%Ti wt.% of the developed HTMMC composition. According to contour plot Fig. 6 (a–c), the process parameter has a greater impact on the response than the weight percentage of reinforcements. Additionally, as demonstrated in Fig. 6 (a–c), enhancing the amount of every process factor (for example, compression pressure and time, milling duration, sintering temperature, and time) considerably enhances the porosity level score and is recommended that they be kept to a minimum for high-quality and high-performance engineering material development. The plot of optimization in Fig. 7 illustrates that the relationship between process variables and response porosity is visible, suggesting that porosity is reliant on the mathematical model.

According to Figs. 4, 5, 6 and 7, bigger process parameter values comprised value for this experimentation developed are a highly significant source for minimizing and managing the porosity of manufactured HTMMC technical material for aerospace and automobile applications. Figure 7 shows the optimized value of optimization using PM via RSM for experiment design of process variables (milling period, compaction pressure, compact duration, sintering temperature, and time) of 6, 50MPa, 50 min,1200°C, and 2h. This outcome was consistent with prior research [25].

Parametric optimization using ANN

ANN is made up of hidden, input, and output levels, with nodes that serve as inputs gathering user data and passing it through hidden layers that vary in size depending on the breadth of the data [26, 27]. The configuration for this inquiry is shown in Table 7 ANN parameters for operation.

The porosity prediction model for this inquiry development strategy was the ANN (Fig. 8) setup (6-10-1 configuration).

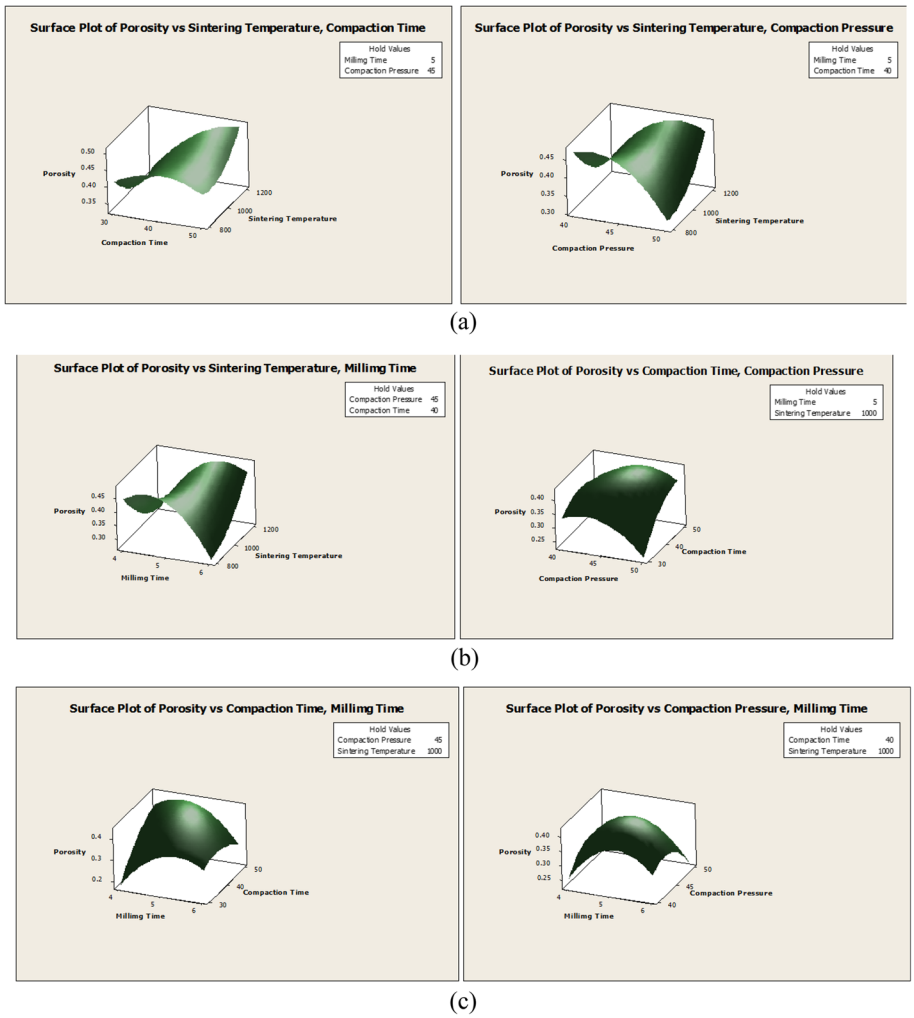

Fig. 5 Surface plot of porosity investigation utilizing PM Process variable RSM for experiment design (**a**–**c**)

Testing and training networks

Training and testing are the two processes in the construction of an ANN model. The network's weights are modified throughout the learning phase to close the gap between anticipated outputs and desired goals [28, 29]. The network was trained using an ANN model of feedback propagation. For learning and testing, the MATLAB 2019b software was utilized, along with data on porosity and density. The Levenberg-Marquardt (LM) method was chosen for reliability and processing time 30].

As a result, the model that was trained predicted with little error, and it can be utilized as well for predicting the unidentified quantity for the next set of data. As demonstrated in Fig. 9, the network was effectively trained with a near-unit determination coefficient ($R = 0.99914$), showing greater performance. The coefficient of regression (R) is closer to one, suggesting better performance. The ANN-predicted values are closer to the experimental values, indicating the modest deviation or very small margin of error. As a result, the proposed model can well anticipate the porosity and experimental density of HTMMC composites.

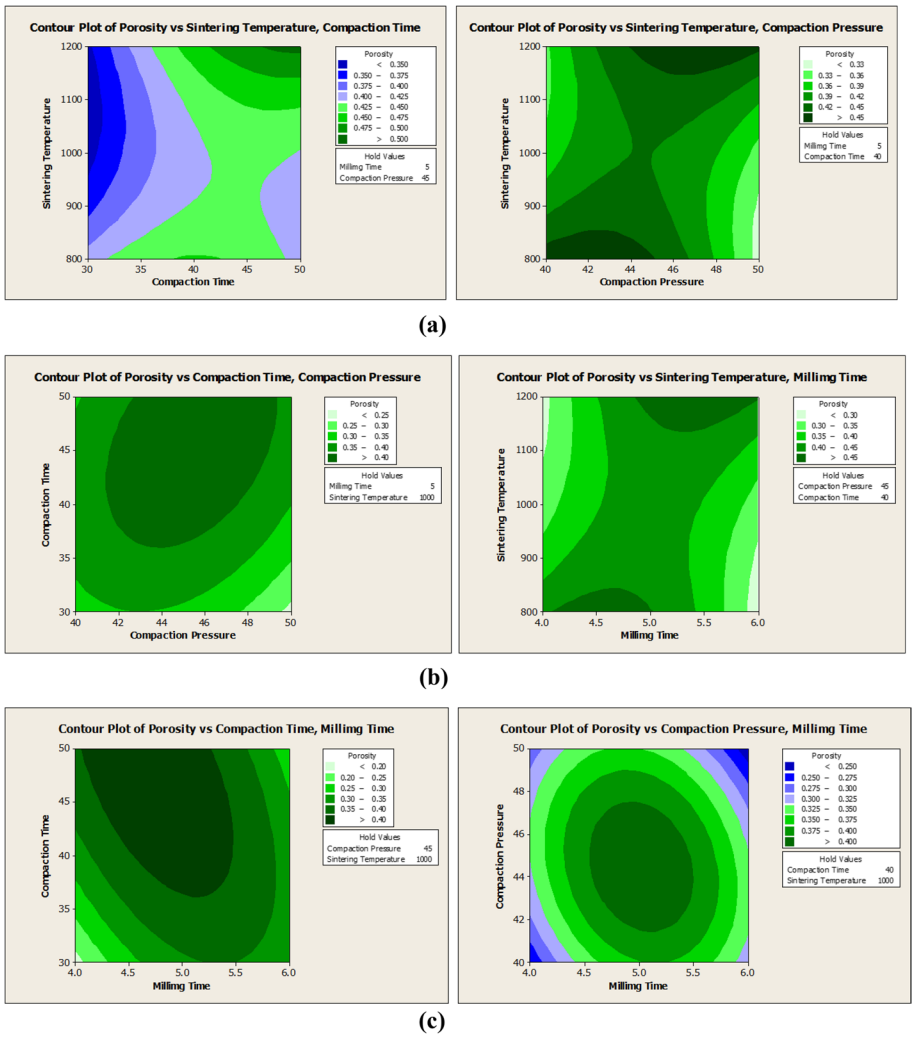

Fig. 6 Contour plot of porosity investigation utilizing PM Process variable RSM for experiment design (**a**–**c**)

The graphic depicts the optimum outcome, shown by a dashed line, where outputs equal goals. A solid line is the best-fitting linear regression line, and the R value reflects the relationship between outputs and goals. If $R = 1$, the relationship is accurate; however, R close to 0 indicates that there is no linear relationship.

The data are all well-fitting, as shown by Fig. 9, which was verified by Jiang and Friedrich et al. [31]. As a result, the trained network system provides results with a minimal proportion of error and may be used to anticipate unknown future values. Input with high agreement between experimental and anticipated values is shown in Fig. 9. Additionally, it verifies that the data is well fitted as a result of proper training. Additionally, the network provides the lowest possible error rate and is utilized to predict future values that are unknown. The R^2 value in the network is very near to 1, indicating that there is very little error [32].

Figure 9 differentiates experimental and anticipated data sets from training, validation, testing, and combined sets. All of the data sets are shown in the corresponding

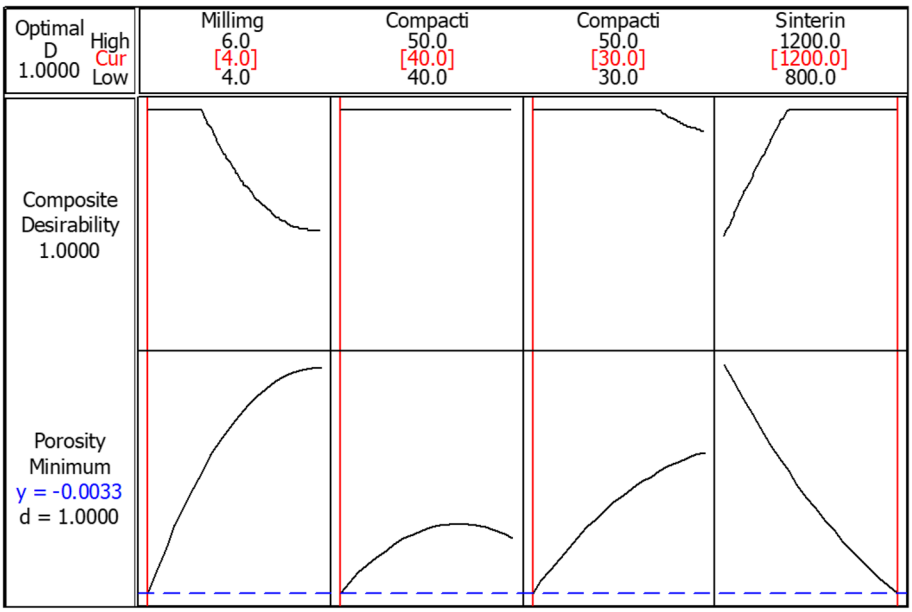

Fig. 7 Porosity investigation optimization utilizing PM via RSM for experiment design of process variables (milling period, compaction pressure, compact duration, sintering temperature, and time)

Table 7 ANN parameters for operation

S. No.	Composition source	Type
1	Configuration of a network	6.10.1
3	The number of hidden neurons	10
2	The number of hidden layers	1
5	The number of patterns utilized for training	9
6	The number of patterns tested and validated	4
7	The number of epochs is 1000	1000
4	The transfer function was utilized	Logsig/sigmoid

graph. The experimental and anticipated output systems are all in good agreement with each other.

The performance status of five input parameters is depicted in Fig. 10. Before the validation curve, the test curve grew noticeably, and it is conceivable that some overfitting had place. This is fixed by continuing the training for a few more iterations before ending. Better outcomes were obtained after retraining the network, which was terminated at the highest regression coefficient value. The obtained *R* values are 0.99914 and 0.95747 after successive training. In both times, the MSE value was rather low, and the scatter plot demonstrated better acceptable fits.

The *R* value of 0.99914 implies that there is a high relationship between network and experimental outcomes. For successful prediction models, adequate input parameters are required while training the network. The experimental and anticipated porosity values of the ANN model were exhibited, proving its accuracy in estimating experimental findings. The use of fewer parameters might result in inefficient models.

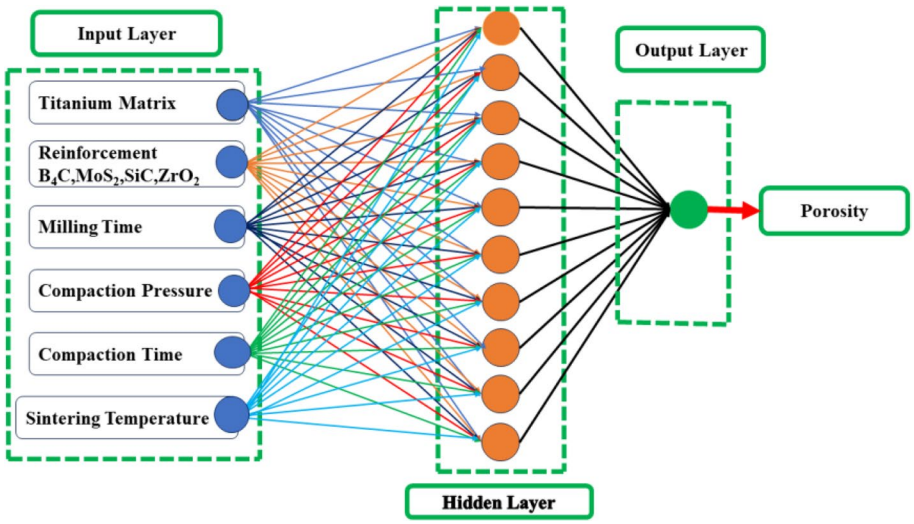

Fig. 8 Neural network architecture designs (6-10-1 configuration) employed as the porosity prediction model

Model verification

The 0.0001 expected error values were considered acceptable and appropriate for ANN training. Figure 10 displays the amount of repetition dependent variations of mistakes for an ANN selected for an optimal amount of reinforced particle. The most effective verification effectiveness and efficiency accuracy could be achieved with three epochs, and the network built attains coherence and reliability despite fewer epochs. During validating the average ANN from all of the training and tested configurations, achievement error was 0.232%, 0.143%, and 0.304% for experimental density, porosity, and hardness, respectively. ANN is a useful technique for predicting the porousness and hardness of materials [30].

Parametric optimization using genetic algorithm

Genetic algorithms (GAs) are particularly advantageous for accomplishing the same, and a program was built to assist the method, as are search algorithms that replicate genomic evolution in biological systems, allowing them to deal with complicated issues that include discontinuous, multi-modal, non-differentiable objective functions. They employ a survival of the fittest strategy, evaluating all stages in the stage space and employing mutation, crossover, and selection procedures to discover optimal solutions for linear and nonlinear problems [21].

The parameters that follow have been chosen to produce best results with little computing effort:

Population size = 50
Population type = double vector
Creation function = constrain dependent
Scaling function = rank
Selection operator = Roulette wheel

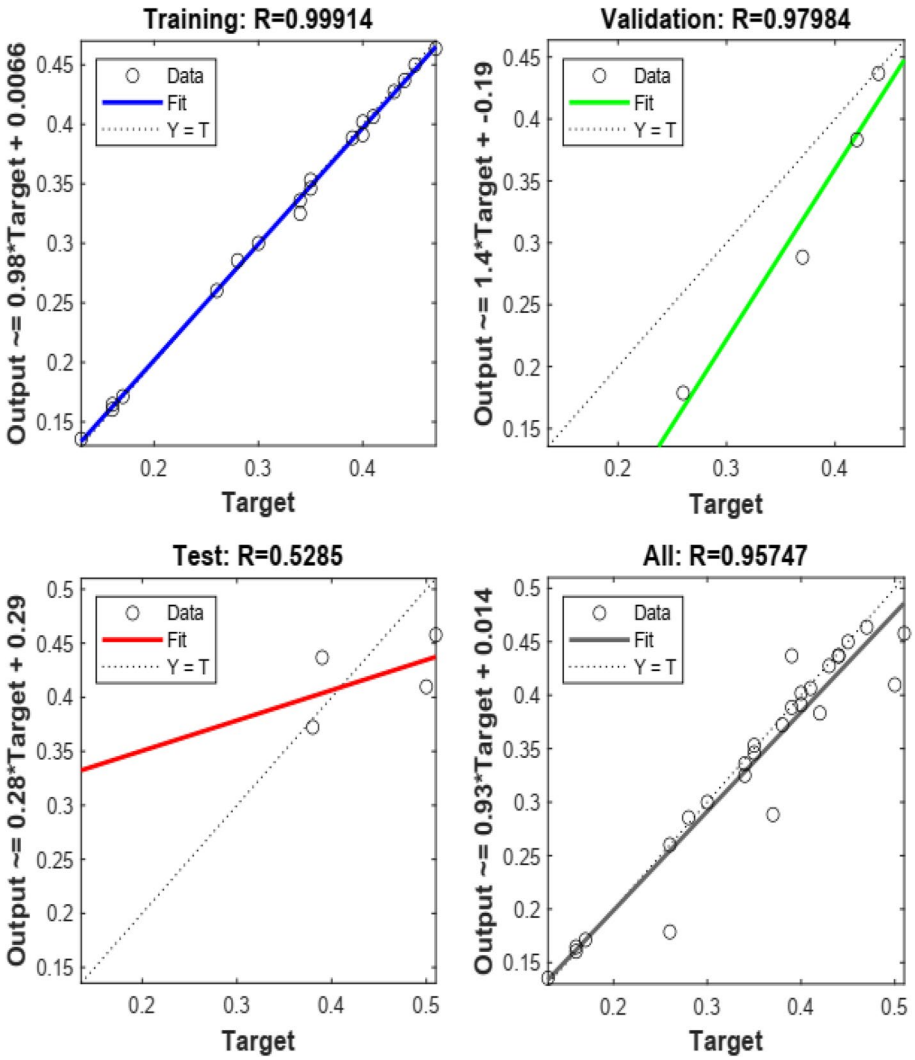

Fig. 9 Predictive analysis regression plots for the constructed network's training, validation, and testing

Elite count = 0.05 * population size
Cross over fraction = 0.8
Mutation function = constrain dependent
Number of generations 100

The study's goal is to use genetic algorithms (GAs) to create a trustworthy approach to predicting powder metallurgy circumstances. GAs was searching algorithms that may solve complicated problems having inconsistent, multi-modal, and non-differentiable purposes through mimicking the evolution of genomics in biological networks. Using the "survival of the fittest" technique, the program seeks to both preserve and utilize the solution population [33, 34]. According to Sheelwant et al. [21], apply GAs to produce a trustworthy strategy to forecast porosity conditions owing to global optimal optimization concede with this optimum result conclusion as shown in Fig. 11 GA analysis.

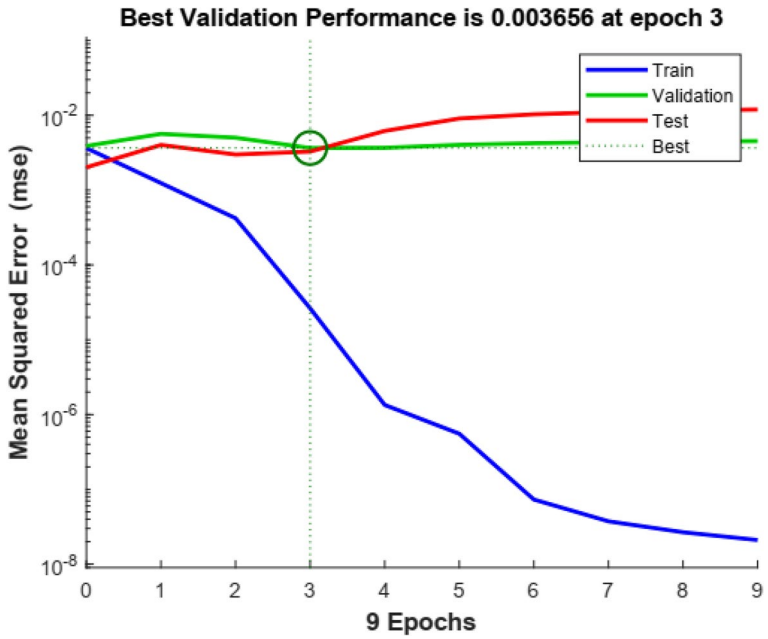

Fig. 10 The resulting performance of the model curves (mean squared error (MSE) vs. epoch number)

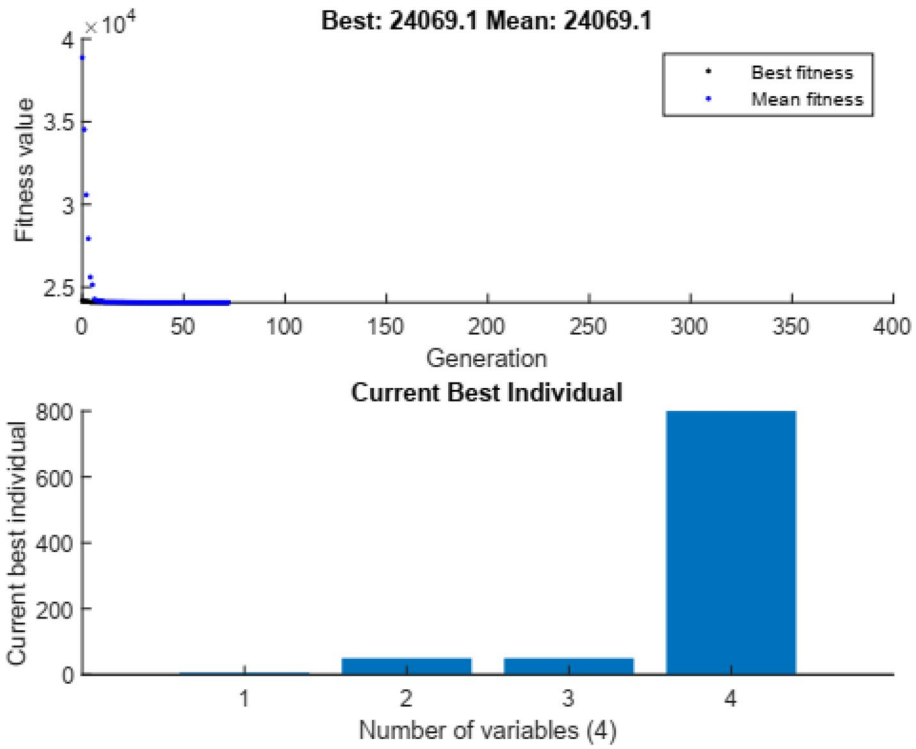

Fig. 11 GA analysis

Experiment confirmation of optimal process variable circumstances

The validation test evaluated the HTMMCS's experimental density, porosity, and Rockwell hardness. RSM was found to be useful for multi-output optimization in

Table 8 Results of the mathematical optimization procedure and composite desirability ratings

Composition of HTMMCs	Powder metallurgy process parameter optimal combination	Number of trial	Experimental density (gm/cm^3)	Porosity (%)	Desirability
7.5% SiC, 7.5% B_4C, 4% MoS_2, 7.5% ZrO_2, 73.5% Ti wt.%	Process variables (milling period, compaction pressure, compact duration, sintering temperature, and time) of 6hrs, 50MPa, 50minute, 1200°C, and 2hrs, respectively	1	4.39	0.0123	0.78368
		2	4.46	0.0117	0.73921
		3	4.24	0.0114	0.76145

Table 9 Experimental validation under optimum circumstances

Run	Sintered sample density (g/cm^3)			Porosity of fabricated optimal Sample (%)		
	Experimental density (gm/cm^3)	Predicted	Error (%)	Experimental porosity	Predicted	Error (%)
1	4.39	4.43	0.04	0.0123	0.0135	0.007
2	4.46	4.49	0.03	0.0117	0.0123	0.004
3	4.24	4.29	0.05	0.0114	0.0116	0.002
Mean			0.04			0.004
Standard deviation			0.081			0.003

biomedical devices, vehicles, and aircraft components, predicting physic mechanical characteristics. This study verifies and aligns with prior findings [15]. Two further trials were performed under the identical settings as solution to check the correctness of the optimal condition provided using response surface methods. Table 8 shows the results of several trials and projected that the response findings in solution carried out three replications for optimal sample composition and process parameters are identical to the observed findings. A mean wt.% error occurred in experimental porosity; experimental density and the experimental Rockwell hardness are 0.004, 0.04, and 1.19, respectively. These data show that the values for the reactions provided by experimentation and anticipated by RSM tool of Design-Expert software are equivalent. As a result, the precision of the optimum settings generated by the computer algorithm is confirmed through actual laboratory experimentation.

The most favorable input variable circumstances have been figured out by computing the quadratic model projection equations based on experimentation data and analyzing the response surface graph. Table 9 shows the input factors and response with the greatest degree of accuracy, with desirability values of 0.78368, 0.76145, and 0.73921, when the three best potential alternatives are considered and experiments are performed with optimal sample composition and process variable optimized result prediction conditions. Desirability scale span/range between 0 and 1, determined by the close proximity for the response to the goal desired outcome [24, 35]. The findings from the experiment were investigated further using ANN and GA with critical analysis and comparison with RSM.

Comparison of integrated ANN-GA and RSM results for HTMMC composite

Integrated ANN-GA results with RSM results are constituted algorithms for predictions that can solve multidimensional nonlinear and linear interaction issues. Previous investigation has shown that integrated ANN-GA results with RSM results are effective tools for estimating process parameters throughout the manufacture of composite materials [33, 36]. These mathematical frameworks have been employed to determine the influence of the input factors on the outcome variables as well as to define variable relationships.

According to Table 10, the R^2 values of 0.9552 and 0.97984 for the RSM and integrated ANN-GA results, respectively, indicate that the RSM forecast has a greater divergence than the integrated ANN-GA projection, indicating that statistical analysis errors were analyzed to compare the projected data.

Its assessment of anticipated integrated ANN-GA and RSM results values is illustrated extensively through result. The outcomes demonstrated how the integrated ANN-GA model is superior than the RSM model for analyzing interaction factors and projections. With an interval of confidence of 95%, the contrast of the findings was shown to predict the porosity near to experimentally collected measurements.

Accordingly, Table 10 shows that the integrated ANN-GA model estimate is more reliable and accurate than the RSM model computation, indicating that ANN has superior capabilities for modeling. A few studies from recently published studies [17, 37] confirm this conclusion. The study used combined ANN-GA findings to forecast and optimize porosity in the production of titanium-based particulate MMCs. The global optimal findings demonstrated that the combined ANN-GA technique considerably improved the manufacturing usability of titanium-based particulate MMCs, indicating its usefulness in the sector.

Synthesized optimized HTMMC characterization

HTMMC XRD analysis

The phase identification and occurrence of reinforcement particles made of B_4C, SiC, MoS_2, and ZrO_2 in the synthesized sintered composites were investigated using an XRD. Figure 12 shows an XRD plot of produced composites with varying B_4C, SiC, MoS_2, and ZrO_2 concentrations. The appropriate peaks found on the XRD graph confirmed the occurrence of titanium and B_4C, SiC, MoS_2, and ZrO_2. Titanium had the largest intensity, because of the highest concentration compared to B_4C, SiC, MoS_2, and ZrO_2. The result revealed a new TiC and TiB peak, showing that a new phase was produced during the sintering process due to the reaction between pure Ti and B_4C. High score plus and

Table 10 RSM vs. integrated ANN-GA comparison

S. No.	Prediction of errors	Porosity of the response surface	
		RSM	Integrated ANN-GA
3	MAPE	0.59	0.05
2	RMSE	1.837	1.0689
1	R^2	*0.9552*	*0.97984*

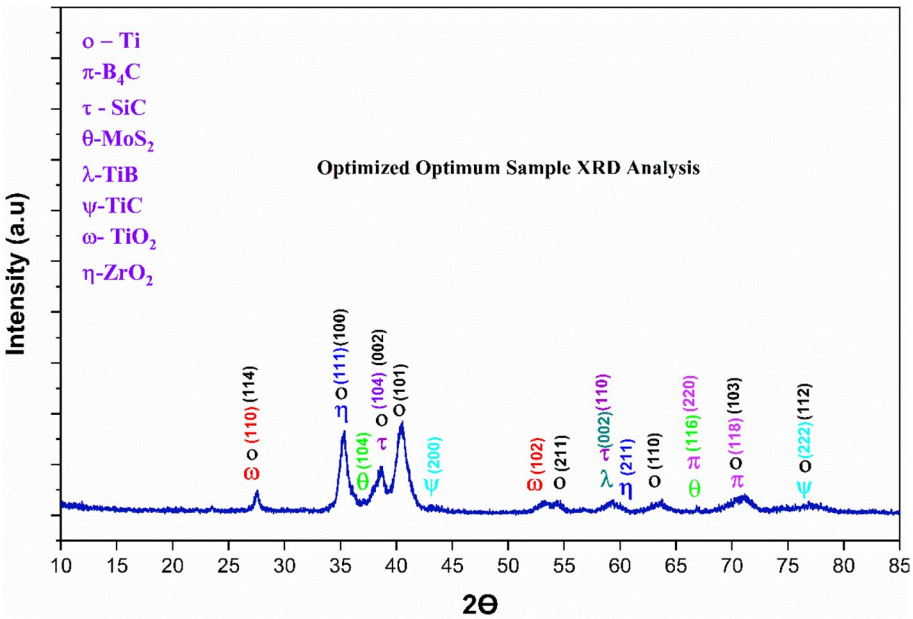

Fig. 12 XRD analyses of optimum samples (OS)

origin software was used to perform the computations. The found results are compatible with the findings of previous studies [38–40].

The XRD pattern of HTMMCs after sintering is shown in Fig. 12. All specimens showed TiO_2 peaks at 2θ = 41.6°, 27.44°, 44.08°, 84.34°, and 79.9°, in accordance with (002), (110), (210), (400), and (212), Miller indices (JCPDS: 021-1276). TiB peaks were detected at 2θ=58.8°, associated to the (002) Miller index (JCPDS: 0044598). The SiC peaks were found at 2θ = 62.78°, 41.28°, and 76.6°, which match the (110), (200), and (103) Miller indices (JCPDS: 049-1623). MoS_2 peaks were found at 2θ= 66.48° and 38.22°, which coincide with the (116) and (104) Miller indices (JCPDS: 0076370). The B_4C peak maxima fit crystallographic patterns with angles 2θ = 69.84°, which matches the (220) Miller indices (JCPDS:00-026-0233). The XRD pattern revealed TiC peaks at 2θ = 36.3° and 41.27°, which coincide to the (111) and (200) Miller indexes (JCPDS: 089-3828). ZrO_2 maxima may be detected at 2θ = 27.5° and 64.1° angles, which align with crystal orientation (111) and (211) Miller indices (JCPDS: 00-037-1484). While extremely rare circumstances, TiC, TiB_2, and TiO_2 appear as new phases while sintering synthetic HTMMC specimens detected by XRD analysis.

Fourier transform infrared spectrometry of fabricated HTMMCs

FTIR spectroscopy is a high-precision, user-friendly instrument for evaluating specimen development and quality, as well as ensuring material absorption and according to ASTM E168 and E1252 standard conformance. Figure 13 shows the FTIR of produced HTMMCs as a consequence of optimal sample experimentation.

The main peak significance for B4C is about 1100 cm^{-1} (more particularly, 1097 cm^{-1} and 1107 cm^{-1} were allocated correctly after comparing with previously published infrared investigations of B-C chemical bonds) [40]. Romanos et al. [40] discovered that the

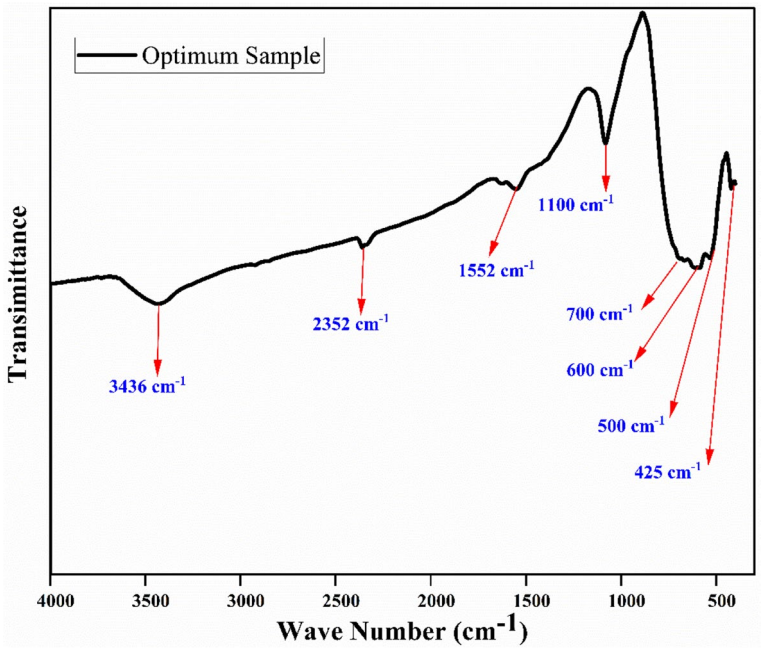

Fig. 13 FTIR of fabricated HTMMCs

acquired peaks coincided with the infrared spectra of the boron-carbon bonds. The SiC platform is responsible for the highest points at 1022 cm^{-1}, 1058 cm^{-1}, 992 cm^{-1} (Si-O), and 700 cm^{-1} (Si-C), which is consistent with the findings of [41]. Prominent peaks were found about 500 cm^{-1} coinciding to the Zr-O stretching vibration of the ZrO_2 phase [42], confirming the development of ZrO_2 as crystallographic phases [43]. Based on the results of the inquiry, the peaks were provided together with the functional groups responsible for TiO_2 synthesis, which could be represented as 420 cm^{-1}, 410 cm^{-1} intramolecular bonded (weak), and 425 cm^{-1} intramolecular bonded (strong). This investigation confirmed the conclusions of [44]. The Mo-S vibration peak is around 600 cm^{-1}, which decreases as spectrum increases, indicating a weaker Mo-S bond [45].

As a result, the primary peak importance for B4C is around 1100 cm^{-1}, which was accurately assigned, and it was discovered that the obtained peaks agreed with the B-C bonds' infrared spectra. At 700 cm^{-1} (Si-C), the SiC platform had the highest scores. Significant peaks were discovered at 500 cm^{-1}, which corresponded with the Zr-O stretching vibration of the ZrO_2 phase and verified the crystallographic phase formation of ZrO_2. As the spectrum widens, the peak of the Mo-S vibration decreases to around 600 cm^{-1}. The functional groups responsible for TiO_2 production, which might be represented as 425 cm^{-1} intramolecular bound (strong) of Ti-O, were offered together with the peaks based on the inquiry's results.

Microstructure analysis

The morphology of the fabricated sample was studied utilizing SEM examining to analyze its SEM micrography that was determined to contain coarse lamellar and separation of phases throughout extreme temperature sintering and followed by slow cooling [46].

In Fig. 14, SEM micrographs revealed that increasing ZrO_2 and B_4C concentrations makes constant MoS_2 and decreasing SiC in the optimum sample (7.5% ZrO_2, 7.5% B_4C, 4% MoS_2, 5% SiC, 76% Ti) reduced porousness and surface densification in HTMMCs. The production of this sophisticated microstructure in the observable micrographs from the created sample SEM morphological concepts has the promise to culminate in some unique properties. The insertion of course, columnar-shaped particles into a fine-grained morphology is unlikely to increase mechanical strength; in fact, it is more likely to cause that region of the part to lose strength [47]. The phase bond was robust in the optimal sample, which had minimum porosity structure between the 76% Ti and 7.5% ZrO_2, 7.5% B_4C, 4% MoS_2, and 5% SiC reinforcement particles. As stated by Harish et al. [48, 49], the quantity of reinforcing particles increases the porousness of MMC material in the morphology. The 1200°C heating temperature resulted in the production of secondary phases, whose presence was visible as darker patches surrounding matrix and reinforcement nanoparticles. The products of these interactions could be seen, but the boundaries of grains were challenging to identify due to the existence of intermetallic and a few pores existed around the particles. Visual analysis proved it difficult to distinguish between secondary phase formations. As a result, these small particles remain embedded throughout the matrix and are immediately identifiable through their dark gray color and angular form. The surface within the amalgamated sample showed fewer brittle cracks and fractures. This behavior was identical to one described and investigated within a previous investigation [50, 51].

Density and porosity analysis The density of composite components is affected by reinforcing elements, phase and size, and manufacturing processes. The porosity investigation process follows the Archimedes principles and the approved mixing rule utilizing Eq. (3). A tumbler was used to submerge and soak the specimen in hot water at 70°C for 2h in order to determine the quantity of compacting and sintered material.

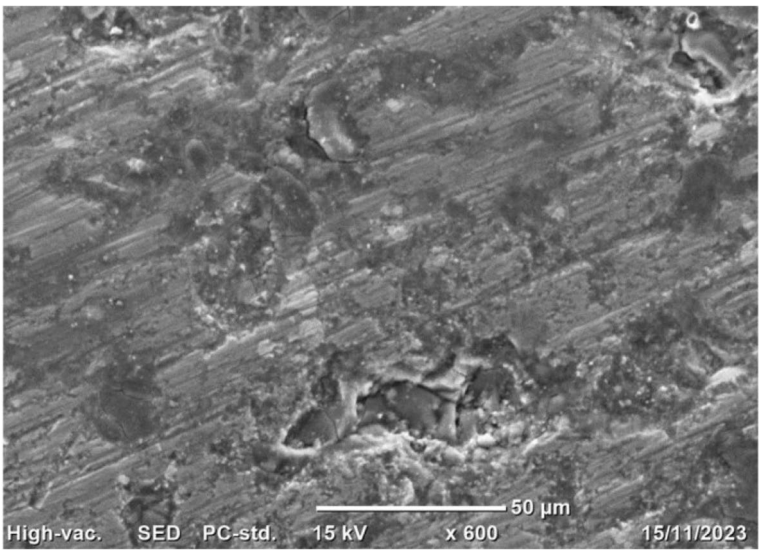

Fig. 14 SEM morphological concepts of developed HTMMC with the composition of 7.5% ZrO_2, 7.5% B_4C, 4% MoS_2, 5% SiC, and 76% Ti through powder metallurgy

Table 11 provides a clear and concise representation of the density and porosity of the optimized sample. However, in accordance with ASTM C 373-72, 1984, the densities of sintered materials are ascertained by applying the Archimedes principle. Using the subsequent formula (2):

$$\rho_{\text{Arch}} = \left\{ \frac{W_{air}}{(W_{air} - W_{\text{liquid}})} \right\} X \rho_{\text{Water}} \tag{2}$$

$$P = \frac{1 - \rho t}{\rho a} \tag{3}$$

where P represents the porosity occurring in the material, ρ_a represents its actual density, and ρ_t represents its theoretical density.

Table 11 shows that the synthesized TMC's low void content and high relative density which indicate strong interface bonding and minimum porosity make it appropriate for use in the automotive and aerospace engineering industries.

Micro-hardness analysis In the industrial industry, Rockwell hardness tests are commonly performed using diamond indenters to get different ISO 6508-1 scales. More precise calibration methods for Rockwell hardness examination devices are yet required by the industry. The Rockwell hardness tester scale was utilized to calculate specimen hardness numbers in accordance with ASTM E18 and 28 standard testing protocols as shown in table 12. A 150-kg Brale indenter was employed, and the load application duration was 15 s.

Table 11 Optimal sample density and porosity analysis result

Composition of HTMMCs	Number of trial	Experimental density (gm/cm^3)	Porosity (%)
7.5% SiC, 7.5% B4C, 4% MoS2, 7.5% ZrO2, 73.5% Ti wt.%	1	4.39	0.0123
	2	4.46	0.0117
	3	4.24	0.0114
Average		**4.36**	**0.0118**

Table 12 Optimal sample micro-hardness analysis result

Composition of HTMMCs	Number of Trial	Rockwell Hardness Type "C" HRC values
7.5% SiC, 7.5% B4C, 4% MoS2, 7.5% ZrO2, 73.5% Ti wt.%	1	67.8
	2	67.9
	3	54.4
Average		**63.4**

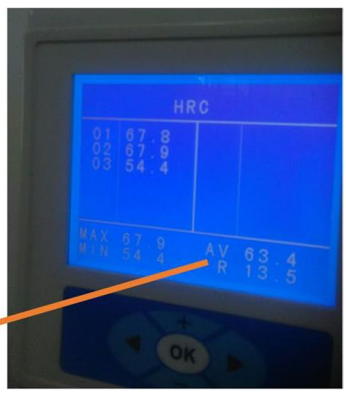

Table 5 demonstrates how the composition of ZrO_2, MoS_2, B_4C, and SiC nanoparticles considerably affects the hardness value of HTMC material. With an increase in sintering temperature or heat, the composition of reinforced B_4C, MoS_2, SiC, and ZrO_2 nanoparticles increases. At 7.5% SiC, 7.5% B_4C, 4% MoS_2, 7.5% ZrO_2, and 73.5% Ti weight percentage, the optimum sample exhibits the greatest hardness of 63.4HRC, showing outstanding mechanical characteristics and densification. Additionally, high-hardness ceramics reinforced and the phase development of TiC and TiB in the matrix are responsible for this, which increases the load-bearing capacity.

Compression strength analysis

The results of the study demonstrate that compositions containing B_4C, SiC, MoS_2, and ZrO_2 hard ceramics have composite compressive strengths that are much greater due to characteristics such matrix structure, equal dispersion of reinforcement particles, higher reinforcement phase, and Orowan reinforcing mechanism. Stronger barriers to dislocation motion are produced by larger grain sizes and grain boundaries as a result of increased atomic diffusion brought on by higher sintering temperatures. In addition, the composites exhibit enhanced mechanical characteristics and high denitrification.

This work investigates the effects of sintering temperature and hard ceramic reinforcement on the compressive strength of composites. Higher sintering temperatures result in stronger reinforcing phases, better matrix structures, and higher compressive strengths; grade 5 pure titanium, on the other hand, has lesser strength. The compressive strength rises to 2500MPa, a 2.6% improvement, when the optimal reinforcing particles 7.5% SiC, 7.5% B_4C, 4% MoS_2, 7.5% ZrO_2, and 73.5% Ti are utilized.

Wear rate analysis

The study investigated the consolidation of composites in dry, room-temperature conditions utilizing Ti-B4C-SiC-MoS2-ZrO2. According to ASTM-G-99 requirements, sample size Ø6X12 mm was tested against Ø120 mm EN31 steel disc with a 65HRC hardness after being exposed to 10N stresses and a 300 rev/min sliding velocity at 1800 m sliding distance. The results have shown that under normal load conditions, a larger indenter dispersion raises the sliding wear rate in Ti alloy. To enhance wear rate resistance, strong ceramic was included into the Ti matrix. Surface modification was caused by an increase in sliding wear rates with an increase in sliding velocity frequency. Titanium was shielded from wear and attrition by the robust ceramic armored plate, and wear loss in the Ti alloy decreased as the concentration of B_4C-SiC-MoS_2-ZrO_2 rose.

The wear rate was significantly improved to 0.176mm^3/N.m when the proper reinforcing particles were utilized. HTMMCs are used in 7.5% SiC, 7.5% B_4C, 4% MoS_2, 7.5% ZrO_2, and 73.5% of these samples; the results are in line with the hardness of the optimally produced samples as shown in table 13. Wear rate investigations found that TiB_2

Table 13 Optimal sample wear rate analysis result

S. No.	Validation examination outcomes	Measured responses data				
		Trial-1	Trial-2	Trial-3	Average response value	Sliding distance
1	Wear rate (WR) mm^3/N.m	0.178	0.175	0.176	0.176	1800m

concentration increased wear rate, but the coefficient of friction showed an opposite trend. Similarly, when the sliding speed of the counter plate rotation increased, the wear rate decreased and the coefficient of friction (COF) increased [52].

The important factor influencing the wear rate amount was load. Based on the results of an optimal sample of SEM micrograph, the wear rate mechanism deformation analysis is displayed in Fig. 15.

Hybrid TMC nanocomposite corrosion behavior analysis

The behavior of electrochemical corrosion Electrochemical impedance spectroscopy (EIS) is a high-performance method used to study material characteristics and electrochemical systems by perturbing the electric potential with a variable frequency sine wave and monitoring the current response within the electrochemical cell. It investigates the interfacial properties of metallic alloy surfaces and advantages from being a steady state approach, sensing tiny signals and probing from 100 mHz to 100 KHz. Electrochemical measurements were carried out in a standard three electrode electrochemical cell (modified from ASTM: G3-89) comprising 3.5 wt% NaCl solution at the temperature of the body (37 ± 2 °C) as one of the key elements of physiological solutions [53].

The potentiodynamic polarization Potentiodynamic polarization experiments and electrochemical impedance spectroscopy (EIS) in 3.5%NaCl aqueous solutions were used to assess the corrosion resistance of synthesized HTMMCs. The corrosion properties of

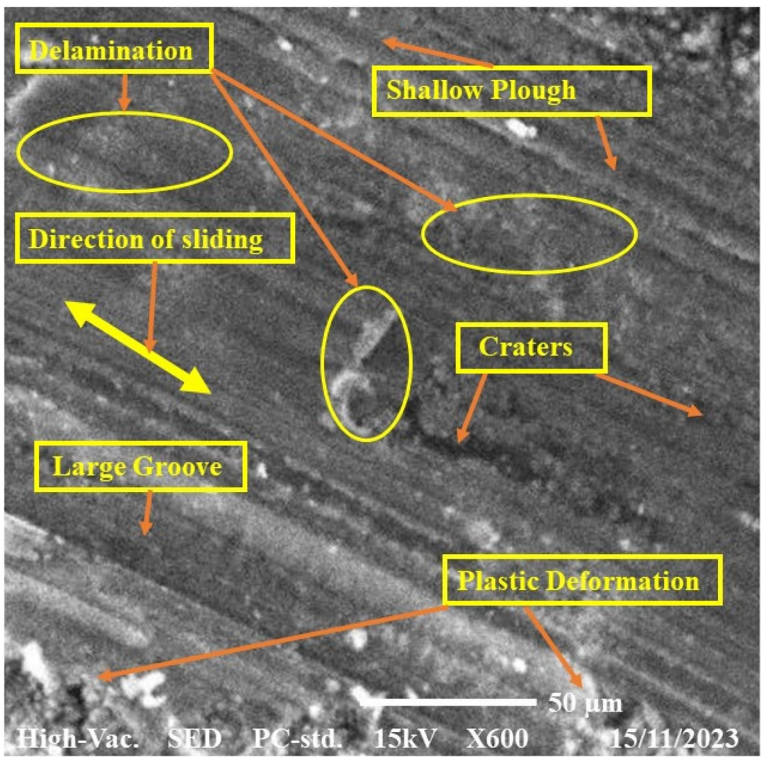

Fig. 15 Wear rate morphology analysis

pure titanium grade 5 base metal matrixes were also compared in the study. An AC current potential was used to set the corrosion potential of the operational electrode after the sample had been stabilized at the corrosion potential (E_{corr}) for 2h. The frequency range for which impedance spectra were gathered was 100 kHz up to 0.01Hz. The experiments were conducted to investigate the corrosion capability of synthesized HTMMCs using an electrochemical analysis machine (BioLogic, Model-SP-200, France).

The retrieved values from the schemes are the corrosion rate (CR), polarization resistance (RP), corrosion potential (Ecorr), and corrosion current density (Icorr). The investigation discovered that greater corrosion resistance resulted from higher corrosion potential and lower current density, with high Ecorr and low Icorr indicating low corrosion rate and confirming the potential for advancement with different scholars.

According to Table 14 that has shown best results, because of its smaller average pore size, fewer cracks, and relatively dense surface microstructure of Ti and HTMMCs, the pure Ti sample has the highest corrosion potential of −0.85V and the lowest corrosion current density of 4.9×10^{-7} Acm^{-2}. For the HTMMCs, on the other hand, the highest corrosion potential of −0.64V and the lowest corrosion current density of 4.8×10^{-10} Acm^{-2} are obtained. The formation of oxide layer and ceramics may reduce the Icorr of pure titanium from 4.9×10^{-7} to 4.8×10^{-10} Acm^{-2} for HTMC optimal sample. This is about 999 times lower than that of titanium metal matrix.

According to Verma et al. [54], the polarization resistance (RP) of the specimens was also established using the Stern-Geary Eq. (4):

$$\mathrm{Rp} = \frac{\beta a \beta c}{2.303 Icorr(\beta a + \beta c)} \tag{4}$$

When the anodic and cathodic slopes of the polarization curves are represented by βa and βc, respectively, the potential for corrosion can be increased while the current density is decreased to predict enhanced corrosion resistance. In addition to more uniform corrosion and a strong corrosion resistance function, high Ecorr and low Icorr suggest a low corrosion rate. The inhibitory efficiency (IE%) of the HTMMC was determined using the following formula (5):

$$\mathrm{InhibitorEfficiency} = \left\{ \frac{I^m corr - \mathrm{I}corr}{I^m corr} \right\} \times 100 \tag{5}$$

where $I^m corr$ is corrosion current density values of pure Ti and Icorr corrosion current density values of HTMMCs.

The maximum inhibitory efficacy of 99.9% is displayed by the optimal sample. This is among the benefits of powder metallurgy fabrication process. Additionally consistent with XRD, Rockwell hardness, compressive strength, and wear rate are these results.

Table 14 Corrosion extrapolation of HTMMC specimens

Samples	Ecor (mV)	Icorr (μA/cm²)	βc (mV)	βa (mV)	RP (Ω)	CR (mm/y)	(IE%)
Pure titanium	−0.85	4.9×10^{-7}	213.3	18.9	1.54×10^{4}	1.7×10^{-2}	0
Optimum sample	−0.64	4.8×10^{-10}	120.98	141.58	5.9×10^{7}	2.15×10^{-4}	99.9

The physical barriers of B_4C, MoS_2, SiC, and ZrO_2 nanoparticle reinforcements are significant and contribute significantly to the enhanced and prevent rate of corrosion of HTMMCs.

Since there are no pores and complete densification, the nano-composites with the optimum sample composition exhibit the lowest corrosion rate. Due to the ceramic particles' reduced reactivity and their homogeneous distribution throughout the Ti matrix, which functions as an internal passive material to lower the corrosion rate, the addition of B_4C, SiC, MoS_2, and ZrO_2 greatly increases the corrosion resistance of hybrid TMC nano-composites with the composition of 7.5% ZrO_2, 7.5% B_4C, 4% MoS_2, 5% SiC, and 76% Ti optimum samples.

The maximum potential and polarization resistance of optimal samples was due to the homogeneous distribution of hybrid reinforcements, as well as the high hardness and compressive strength of HTMMCs at the specified fraction. According to Katkar et al. [55]'s mixed potential hypothesis, when the reinforcement content in the HMMCs grows, the HMMC's potential changes in the noble direction.

Electrochemical impedance spectroscopy analysis method Nyquist strategies were produced 2h after submerging Ti and HTMMC sample electrodes in 3.5% NaCl solutions. Because of their larger semicircle diameter, the spectra showed that the base metal is less resistant to corrosion than HTMMCs. Higher reinforcing content in HTMMCs results in lower corrosion current possess. According to Shafqat et al. [56], constant phase elements (Q, CPEs) with α value close to 1.0 indicate low porosity double-layer capacitors in all samples. The reason for this is that CPE might resemble Warburg impedance at $\alpha = 0.5$, capacitance at $\alpha = 1$, resistance at $Z(CPE) = R$, and so on, depending on α according to the investigation of Sherif [57]. The characteristics of the equivalent circuit model shown in Fig. 16 can be provided as follows, in accordance with usual practice: Solution resistance is denoted by RS, polarization resistances by Rpa and Rpc, and constant phase elements (CPEs) by Qa and Qc. This suggests that, compared to pure Ti grade 5, HTMMCs have greater corrosion resistance. Due to the higher corrosion resistance of the HTMMC surface over the Ti surface, Table 15 shows that the RS, Rpa, and Rpc values for HTMMCs are larger than those for pure Ti. The admittance and impedance of a CPE are given by the following Eqs. (6) and (7), respectively.

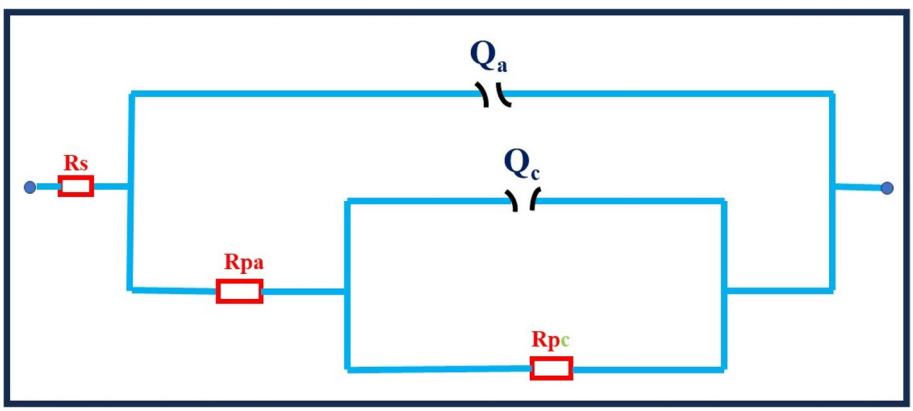

Fig. 16 The equivalent circuit model used to fit the EIS experimental data [53]

Table 15 EIS data combined with the equivalent circuit diagram

Sample	Rs (Ω cm^2)	Qa (μF/cm^2)	Phase ($\alpha_{1)}$	Rpa (Ω cm^2)	Qc (μF/cm^2)	Phase ($\alpha_{2)}$	Rpc (Ω cm^2)
Pure titanium	5.21×10^{2}	7.5×10^{-5}	0.884	1.53×10^{3}	6.1083	0.85	562.35
Optimum sample	8.94×10^{2}	1.6×10^{-6}	0.965	7.5×10^{6}	1.96×10^{-6}	0.989	3.15×10^{7}

$$Y_{CPE} = Y_0[j\omega]^{\alpha} \tag{6}$$

$$Z_{CPE} = \lceil \frac{1}{Y_0} \rceil (j\omega)^{-\alpha} \tag{7}$$

where Y_0-modulus, ω-angular frequency, and α-phase values are ranging from 0 to 1.

Furthermore, the CPE for Ti were higher than those for HTMMCs. By increasing the weight % of secondary reinforcements up to a certain point, more reductions were achieved before it increased once again. Through grain refinement and the creation of a smooth, homogenous HTMMCs, further reinforcements of B_4C, SiC, MoS_2, and ZrO_2 into the Ti matrix increase the anti-corrosion efficiency of HTMMCs. This prevents rusting by serving as a physical barrier layer. The HTMMCs were a stronger and more resilient to matrix disintegration because of the uniform dispersion of nano-reinforcement particles.

Comparing the OS HTMMC sample to other HTMMCs and Ti, EIS tests reveal that it has greater surface passivation and improved corrosion resistance. Potentiodynamic polarization experiments yielded results that are in excellent agreement with the EIS data. In 3.5% NaCl solutions, hybrid reinforced HTMMCs are less prone to uniform and pitting corrosion than the basic material, pure Ti. The degree to which chloride ions inhibit corrosion is lessened when hybrid reinforcements are increased.

The EIS results for pure Ti and optimum sample are listed in Table 15. The results for HTMMCs are Rs = 8.94×10^{2} Ω cm^2, Rpa = 7.5×106 cm^2, and Rpc = 3.15×10^{7} Ω cm^2, whereas the figures for pure Ti substrate are Rs = 5.21×10^{2} Ω cm^2, Rpa = 1.53×10^{3} Ω cm^2, and Rpc = 562.35 Ω cm^2. Since the Rpc values are significantly higher, the results show that the synthesized HTMMCs have a greater corrosion resistance. Investigations of the corrosion properties of Ti and its HTMCs utilizing potentiodynamic polarization and impedance show that the degree of resistance to corrosion of the HTMCs is higher than that of the Ti base metal.

Morphological characterization of after corrosion

As Fig. 17 has shown, the research investigation focuses at the bonding of matrix and B_4C, SiC, MoS_2, and ZrO_2 with the matrix on the uncorroded and corroded surfaces of the optimal sample of HTMMCs. The porous nature of the uncorroded surface corresponds to density and porosity results. The optimum HTMMC sample is less damaged than the pure titanium sample. The inclusion of optimal reinforcing particles (7.5% ZrO_2, 7.5% B_4C, 4% MoS_2, 5% SiC, 76% Ti) results in reduced surface deterioration. Pitting corrosion was reported on pure titanium samples. The joint action of hybrid reinforcement

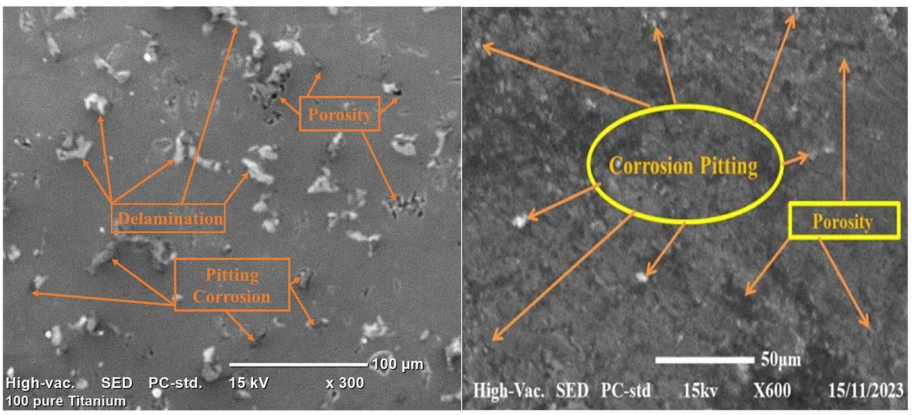

Fig. 17 SEM micrograph of after corrosion test (**a**) 100% pure Ti and (**b**) HTMMC optimum samples (OS)

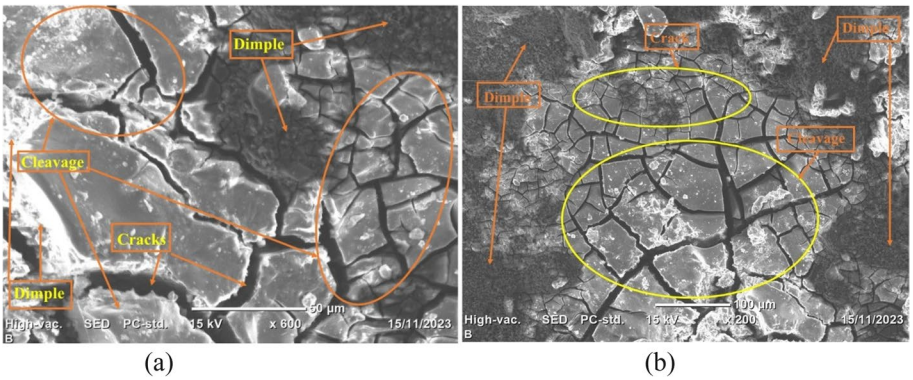

Fig. 18 Fractography analysis of compressed optimal sample. **a** Analysis of the fracture morphology analysis. **b** Surface fracture at low magnification

minimizes pitting susceptibility. Morphological study of SEM micrographs demonstrates that HTMMCs have less damage than the Ti matrix.

The research findings find that hybrid reinforcement particles significantly improved HTMMC corrosion resistance, therefore rendering them acceptable for potential utilization in a variety of industries.

Fractography analysis

A fracture map of the samples' surface morphology is shown in Fig. 18, which shows brittle cracking in the HTMMCs. Pore size changes brought about by agglomeration during powder mixing resulted in a reduction in mechanical properties and a large number of indentations on the micrograph. Small cracks propagated when a force was applied perpendicular to the sample; in certain places, cleavage cracking also occurred, which increased the fracture of composite samples because of their brittle nature. SEM was used to investigate the fracture processes and investigate the micrographs' structure.

The severe failure mode of brittle fracture in titanium alloy, which is used in critical structures, can result in catastrophic incidents when it is caused by a combination of factors such as room temperature creep, hydrogen embrittlement, coupling processes,

oxygen embrittlement, and liquid metal embrittlement. Brittle fractures can begin under the surface or at the surface due to stress levels beyond the threshold value [58]. Compression testing exhibits experience contact surface cracking and eventually succumbs to overstress concentration, emphasizing the need of managing materials properly and preventing failures. The composites' fracture behavior was characterized by dimples, which are typical of ductile fracture, as well as a significant quantity of cleavage planes and grain cracks [13]. SEM examination of the cracked surfaces indicated that unreinforced material fractures simply ductility, whereas reinforced material fractures through crack nucleation and plastic deformation [59].

Figure 18 depicts the fracture as having three regions: region I, which shows small fractures along grain boundaries; region II, which occupies about half of the fracture surface and has cleavage morphological; and region III, which has dimple structure morphological. The fracture has dimple morphology in the margin, axial cracking and cleavage characteristics in the center, and grain boundary cracking surrounding the axial crack. According to the investigation, stress levels over the threshold value can cause brittle fractures to begin under the surface or at the surface. Contact surface cracking during compression testing concentrates the overstress, underscoring the need of effective material management and failure prevention.

Conclusions

The present research investigation focuses at the synthesis, microstructural properties, and porosity behavior of a (2.5, 5, 7.5%) Wt.% B_4C, SiC, and ZrO_2 powder, as well as a 4% MoS_2 fortified Ti composite powder. Powder metallurgy technology used to create sintered composites. The RSM method was utilized for development and designing experiments, modeling and process factor optimization. Furthermore, ANN-GA prediction of porosity for Ti/B_4C-MoS_2-SiC-ZrO_2 composites was done, and the findings matched those obtained by RSM approaches. The following key findings have been made from this analysis.

1. XRD confirmed that the B_4C-MoS_2-SiC-ZrO_2 nanoparticles were contained and identically dispersed in the Ti matrix. The inclusion of B_4C-MoS_2-SiC-ZrO_2 to the produced composites increases the Rockwell microhardness owing to hard ceramics particles. In all compositions, the hardness of the composites was greater than that of the basic Ti.
2. The mechanical properties of optimum combination of 7.5%SiC, 7.5%B4C, 4%MoS_2, 7.5% ZrO_2, and 73.5%Ti wt.% was achieved using process variables (milling period, compaction pressure, compact duration, sintering temperature, and time) of 6h, 50MPa, 50min, 1200°C, and 2h with achieved minimum porosity of 0.118 %, density of 4.36g/cm^3, and microhardness of 63.4HRC enhanced with 1.76%; compressive strength 2500MPa achieved was enhanced with 2.6% when compared with pure Ti. Additionally, the minimum wear rate 0.176mm^3/N.m and corrosion resistance rate 2.15×10-4mmpy achieved these HTMMCs.
3. A quadratic model was created using RSM experimental design to predict the Ti/B_4C-MoS_2-SiC-ZrO_2 composite porosity in terms of B_4C-MoS_2-SiC-ZrO_2 content,

compressive pressure, milling time, and sintering temperature. The model equation response is in great consistent with the observed data.

4. To predict the porosity of the manufactured Ti/B_4C-MoS_2-SiC-ZrO_2 composites, an integrated ANN-GA model was created. The combined ANN-GA model predicts porosity values that are close to the data obtained from experiments.
5. *R*-square values of 0.9552 and 0.97984 (closer to 1) show that the RSM and combined ANN-GA models are substantially linked. This data clearly shows that the RSM prediction deviates more than the ANN-GA forecast combined. The MAPE and RMSE for RSM were 0.59 and 1.837, respectively, whereas the MAPE and RMSE for integrated ANN-GA were 0.050 and 1.0689, respectively. When it comes to examining interactions, variables, and projection, the results reveal that the combined ANN-GA model surpasses RSM.

As a result, when the outcomes predicted by the ANN model were compared to the results of the experiment, they were shown to be accurate. GA is the most accurate global evolutionary optimization approach for fitting experimental findings. In terms of predicting porosity, the created model worked well, and the results presented demonstrate the importance of the combined ANN-GA technique in widening the industrial usage of Ti-based particulate MMCs.

Abbreviations

TMCs	Titanium matrix composites
HTMMCs	Hybrid titanium metal matrix composites
RSM	Response surface methodology
ANN	Artificial neural networks
GA	Genetic algorithm
PM	Powder metallurgy
FTIR	Fourier transform infrared
COF	Coefficient of friction
EIS	Electrochemical impedance spectroscopy

Acknowledgements
Not applicable.

Authors' contributions
All authors have read and approved the manuscript.

Funding
No funding has been done for this research work.

Availability of materials
The datasets used and/or analyzed during the current study are available from the corresponding author on reasonable request.

Declarations

Competing interests
The authors declare no competing interests.

Received: 13 January 2024 Accepted: 18 April 2024
Published online: 15 May 2024

References

1. De D, Nandi T, Bandyopadhyay A (2022) Parametric study using response surface methodology of Ti-Al2O3 (15 vol% of Ti taken as Al2O3 reinforced as alumina fibre into titanium matrix) composite material while undergoing WEDM process. Mater Today 59:A36–A44

2. Penyashki, T., Kamburov, V., Kostadinov, G., Kandeva, M., Dimitrova, R., & Nikolov, A. (2021). Some ways to increase the wear resistance of titanium alloys. J Balkan Tribol Assoc, 27(1). pp 1-20
3. Chirico C, Romero AV, Gordo E, Tsipas SA (2022) Improvement of wear resistance of low-cost powder metallurgy β-titanium alloys for biomedical applications. Surf Coat Technol 434:128207
4. Khanna N, Zadafiya K, Patel T, Kaynak Y, Rashid RAR, Vafadar A (2021) Review on machining of additively manufactured nickel and titanium alloys. J Mater Res Technol 15:3192–3221
5. Wang R, Gu D, Huang G, Shi K, Yuan L, Zhang H (2023) Multilayered gradient titanium-matrix composites fabricated by multi-material laser powder bed fusion using metallized ceramic: forming characteristics, microstructure evolution, and multifunctional properties. Addit Manufact 62:103407
6. Cai C, Radoslaw C, Zhang J, Yan Q, Wen S, Song B, Shi Y (2019) In-situ preparation and formation of TiB/Ti-6Al-4V nanocomposite via laser additive manufacturing: microstructure evolution and tribological behavior. Powder Technol 342:73–84
7. Gonçalves, V. R. M., Corrêa, D. R. N., Grandini, C. R., Pintão, C. A. F., Afonso, C. R. M., & Lisboa Filho, P. N. (2023). Assessment of improved tribocorrosion in novel in-situ Ti and β Ti–40Nb alloy matrix composites produced with NbC addition during arc-melting for biomedical applications. Mater Chem Phys,Vol.301, pp. 127597.
8. Guo S, Li Y, Gu J, Liu J, Peng Y, Wang P, Wang K (2023) Microstructure and mechanical properties of Ti6Al4V/B4C titanium matrix composite fabricated by selective laser melting (SLM). J Mater Res Technol 23:1934–1946
9. Selvakumar M, Chandrasekar P, Mohanraj M, Ravisankar B, Balaraju JN (2015) Role of powder metallurgical processing and TiB reinforcement on mechanical response of Ti–TiB composites. Mater Lett 144:58–61
10. Kondoh, K. (2015). Titanium metal matrix composites by powder metallurgy (PM) routes. In Titanium powder metallurgy (pp. 277-297). Butterworth-Heinemann.
11. Dey D, Bhowmik A, Biswas A (2023) A grey-fuzzy based multi-response optimisation study on the friction and wear characteristics of titanium diboride reinforced aluminium matrix composite. Proc Inst Mechan Eng Part B 237(14):2227–2239
12. Marler RT, Arora JS (2004) Survey of multi-objective optimization methods for engineering. Struct Multidisc Optim 26:369–395
13. Ogunsanya OA, Adewale Akinwande A, Raj Mohan R, et al (2023) Experimental investigation on the mechanical performance of the Al2O3 and ZrO2 added Al-Mg-Si alloy for structural applications. Proc Inst Mech Eng E. https://doi.org/10.1177/09544089231159777
14. Sharma VK, Kumar V, Joshi RS (2020) Parametric study of aluminium-rare earth based composites with improved hydrophobicity using response surface method. J Mater Res Technol 9(3):4919–4932. ISSN 2238-7854. https://doi.org/10.1016/j.jmrt.2020.03.011
15. Khajelakzay M, Bakhshi SR (2017) Optimization of spark plasma sintering parameters of Si3N4-SiC composite using response surface methodology (RSM). Ceram Int 43(9):6815–6821
16. Graupe D (2013) Principles of artificial neural networks, vol 7. World Scientific, Singapore
17. Kannaiyan M, Raghuvaran JGT (2020) Prediction of specific wear rate for LM25/ZrO2 composites using Levenberg–Marquardt backpropagation algorithm. J Mater Res Technol 9(1):530–538
18. Mukhopadhyay A, Barman TK, Sahoo P, Davim JP (2019) Modeling and optimization of fractal dimension in wire electrical discharge machining of EN 31 steel using the ANN-GA approach. Materials 12(3):454
19. Lee D, Morillo C, Oller S, Bugeda G, Oñate E (2013) Robust design optimization of advance hybrid (fiber–metal) composite structures. Composite Structures 99:181–192
20. Elsen SR, Ramesh T (2016) Analysis and optimization of dry sliding wear characteristics of zirconia reinforced alumina composites formed by conventional sintering using response surface method. Int J Refract Met Hard Mater 58:92–103
21. Sheelwant A, Jadhav PM, Narala SKR (2021) ANN-GA based parametric optimization of Al-TiB2 metal matrix composite material processing technique. Mater Today Commun 27:102444
22. Pandey K, Kumar S, Malik A, Kuriqi A (2020) Artificial neural network optimized with a genetic algorithm for seasonal groundwater table depth prediction in Uttar Pradesh India. Sustainabil 12(21):8932
23. Somashekhar KP, Ramachandran N, Mathew J (2010) Optimization of material removal rate in micro-EDM using artificial neural network and genetic algorithms. Mater Manufact Process 25(6):467–475
24. Mahdavi M, Kimiagar S, Abrinaei F (2020) Preparation of few-layered wide bandgap MoS2 with nanometer lateral dimensions by applying laser irradiation. Crystals 10(3):164
25. Alam MA, Hamdan HY, Azeem M, Hussain PB, bin Salit, M. S., Khan, R., … & Ansari, A. H. (2020) Modelling and optimisation of hardness behaviour of sintered Al/SiC composites using RSM and ANN: a comparative study. J Mater Res Technol 9(6):14036–14050
26. Gopalakannan S, Senthilvelan T (2013) Application of response surface method on machining of Al–SiC nanocomposites. Measurement 46(8):2705–2715
27. Varol T, Canakci A, Ozsahin S (2013) Artificial neural network modeling to effect of reinforcement properties on the physical and mechanical properties of Al2024–B4C composites produced by powder metallurgy. Composites Part B: Engineering 54:224–233
28. Arif S, Alam MT, Ansari AH, Shaikh MBN, Siddiqui MA (2018) Analysis of tribological behaviour of zirconia reinforced Al-SiC hybrid composites using statistical and artificial neural network technique. Mater Res Express 5(5):056506
29. Urang JG, Ebong ED, Akpan AE, Akaerue EI (2020) A new approach for porosity and permeability prediction from well logs using artificial neural network and curve fitting techniques: a case study of Niger Delta Nigeria. J Appl Geophys 183:104207
30. Mahanta S, Chandrasekaran M, Samanta S, Arunachalam R (2019) Multi-response ANN modelling and analysis on sliding wear behavior of Al7075/B4C/fly ash hybrid nanocomposites. Mater Res Express 6(8):0850h4
31. Jiang Z, Zhang Z, Friedrich K (2007) Prediction on wear properties of polymer composites with artificial neural networks. Compos Sci Technol 67(2):168–176
32. Muthukrishnan N, Davim JP (2009) Optimization of machining parameters of Al/SiC-MMC with ANOVA and ANN analysis. J Mater Process Technol 209(1):225–232

33. Radhika N, Vijaykarthik KT, Shivaram P (2015) Adhesive wear behaviour of aluminium hybrid metal matrix composites using genetic algorithm. J Eng Sci Technol 10(3):258–268
34. Pandey, A., Yadav, R. N., & Kumar, S. (2016). Modelling and optimization of wire-EDM process using integrated approach of ANN-GA.
35. Meignanamoorthy, M., Vinayagam, M., Ravichandran, M., Raja, T., Gacem, A., Mezni, A., ... & Ganesan, M. (2022). Evaluation on powder metallurgy process parameters of ball-milled AA8079-B4C nanostructured composites via Taguchi grey relational analysis. J Nanomater, 2022.
36. Kumar R, Chauhan S (2015) Study on surface roughness measurement for turning of Al 7075/10/SiCp and Al 7075 hybrid composites by using response surface methodology (RSM) and artificial neural networking (ANN). Measurement 65:166–180
37. Antil SK, Antil P, Singh S, Kumar A, Pruncu CI (2020) Artificial neural network and response surface methodology-based analysis on solid particle erosion behavior of polymer matrix composites. Materials 13(6):1381
38. Nartu MSKKY, Mantri SA, Pantawane MV, Ho YH, McWilliams B, Cho K, Banerjee R (2020) In situ reactions during direct laser deposition of Ti-B4C composites. Scripta Materialia 183:28–32
39. Wang L, Huang Y, Jia C, Yang L, Yan S (2023) Laser-directed energy deposition of in-situ titanium-matrix coatings with a Ti-B4C cored wire. Addit Manufact 73:103682
40. Xiu Z, Ju B, Zhan J, Zhang N, Wang P, Zhao K, Yang W (2023) Microstructure and mechanical properties of core-shell B4C-reinforced Ti matrix composites. Materials 16(3):1166
41. Romanos J, Beckner M, Stalla D, Tekeei A, Suppes G, Jalisatgi S, Pfeifer P (2013) Infrared study of boron–carbon chemical bonds in boron-doped activated carbon. Carbon 54:208–214
42. Chakrabarty K, Chen WC, Baker PA, Vijayan VM, Chen CC, Catledge SA (2020) Super hard boron-rich boron carbide with controlled degree of crystallinity. Materials 13(16):3622
43. Kumar S, Bhunia S (2015) Ojha AK Effect of calcination temperature on phase transformation, structural and optical properties of sol-gel derived ZrO 2 nanostructures. Phys E 66:74–80
44. Horti NC, Kamatagi MD, Nataraj SK, Wari MN, Inamdar SR (2020) Structural and optical properties of zirconium oxide (ZrO2) nanoparticles: effect of calcination temperature. Nano Express 1(1):010022
45. Santhoshkumar T, Rahuman AA, Jayaseelan C, Rajakumar G, Marimuthu S, Kirthi AV, Kim SK (2014) Green synthesis of titanium dioxide nanoparticles using Psidium guajava extract and its antibacterial and antioxidant properties. Asian Pac J Trop Med 7(12):968–976
46. Zhang Z, Topping T, Li Y, Vogt R, Zhou Y, Haines C, Paras J, Kapoor D, Schoenung JM, Lavernia EJ (2011) Mechanical behavior of ultrafine-grained composites reinforced with B4C nanoparticles. Scr Mater 65:652–655. https://doi.org/10.1016/j.scriptamat.2011.06.037
47. Barrie C, Fernandez-Silva B, Snell R, Todd I, Jackson M (2023) AddFAST: A hybrid technique for tailoring microstructures in titanium-titanium composites. J Mater Process Technol 315:117920
48. Henriques VA (2009) Titanium production for aerospace applications. J Aerosp Technol Manag 1:7–17
49. Harish BR, Shaik Dawood AK, Nagabhushan A, Pimpale S, Raja Reddy CV (2016) Comparative study on individual and combined effects of zirconium dioxide and graphite reinforcements on mechanical properties of Al 6061 composites. Int J Res Eng Technol 5:412–416
50. Arevalo C, Montealegre-Melendez I, Ariza E, Kitzmantel M, Rubio-Escudero C, Neubauer E (2016) Influence of sintering temperature on the microstructure and mechanical properties of in situ reinforced titanium composites by inductive hot pressing. Materials 9(11):919
51. Montealegre-Melendez I, Arevalo C, Ariza E, Perez-Soriano EM, Rubio-Escudero C, Kitzmantel M, Neubauer E (2017) Analysis of the microstructure and mechanical properties of titanium-based composites reinforced by secondary phases and B4C particles produced via direct hot pressing. Materials 10(11):1240
52. Bhowmik A, Dey D, Biswas A (2021) Impact of TiB 2 content and sliding velocity on wear performance of aluminium matrix composites. J Sci Indust Res 80(7):600–605
53. Sousa L, Alves AC, Guedes A, Toptan F (2021) Corrosion and tribocorrosion behaviour of Ti-B4C composites processed by conventional sintering and hot-pressing technique. J Alloys Compounds 885:161109
54. Verma AS et al (2015) Corrosion behavior of aluminum base particulate metal matrix composites: a review. Materials Today 2(4):2840–2851. https://doi.org/10.1016/j.matpr.2015.07.299
55. Katkar V et al (2011) Effect of the reinforced boron carbide particulate content of AA6061 alloy on formation of the passive film in seawater. Corros Sci 53:2700–2712. https://doi.org/10.1016/j.corsci.2011.04.023
56. Abbas shafqat Q et al (2019) Mechanical, tribological, and electrochemical behavior of hybrid aluminum matrix composite containing boron carbide (B4C) and graphene nanoplatelets. J Mater Res 34(18):3116–3129. https://doi.org/10.1557/jmr.2019.242
57. Sherif E-SM (2014) A comparative study on the electrochemical corrosion behavior of iron and X-65 steel in 4.0 wt% sodium chloride solution after different exposure intervals. Molecules 19(7):9962–9974
58. Zhang W, Huang Y, Dai W, Jin X, Yin C (2016) A fracture analysis of Ti-10Mo-V-1Fe-3.5Al alloy screw during assembly. Materials 9(10):852
59. Dey D, Bhowmik A, Biswas A (2021) Characterization of physical and mechanical properties of aluminium based composites reinforced with titanium diboride particulates. J Compos Mater 55(14):1979–1991